Geochemistry, Geophysics, Geosystems®

AGU ADVANCING EARTH AND SPACE SCIENCE

RESEARCH ARTICLE
10.1029/2022GC010608

The Mechanical Nature of the Lithosphere Beneath the Eastern Central Atlantic Hotspots

Alberto Jiménez-Díaz[1], Ana M. Negredo[2,3], Jon F. Kirby[4], Pilar Sánchez-Pastor[5], Javier Fullea[2,6], Javier Ruiz[7], Marta Pérez-Gussinyé[8], and Chuanhai Yu[9,10,11]

[1]Departamento de Biología y Geología, Física y Química Inorgánica, ESCET, Universidad Rey Juan Carlos, Madrid, Spain, [2]Departamento de Física de la Tierra y Astrofísica, Facultad de Ciencias Físicas, Universidad Complutense de Madrid, Madrid, Spain, [3]Instituto de Geociencias, IGEO (CSIC, UCM), Madrid, Spain, [4]School of Earth and Planetary Sciences, Curtin University, Perth, WA, Australia, [5]Swiss Seismological Service, ETH Zürich, Zürich, Switzerland, [6]School of Cosmic Physics, Geophysics Section, Dublin Institute for Advanced Studies, Dublin, Ireland, [7]Departamento de Geodinámica, Estratigrafía y Paleontología, Facultad de Ciencias Geológicas, Universidad Complutense de Madrid, Madrid, Spain, [8]MARUM, University of Bremen, Bremen, Germany, [9]Key Laboratory of Ocean and Marginal Sea Geology, South China Sea Institute of Oceanology, Innovation Academy of South China Sea Ecology and Environmental Engineering, Chinese Academy of Sciences, Guangzhou, China, [10]Southern Marine Science and Engineering Guangdong Laboratory (Guangzhou), Guangzhou, China, [11]China-Pakistan Joint Research Center on Earth Sciences, CAS-HEC, Islamabad, Pakistan

Key Points:

- The mechanical effects of the Eastern Central Atlantic hotspots are investigated
- The Azores, Cape Verde, Great Meteor, and Madeira hotspots show standard T_e values
- The Canary hotspot is the notable exception, with a complex pattern of T_e

Supporting Information:

Supporting Information may be found in the online version of this article.

Correspondence to:

A. Jiménez-Díaz and A. M. Negredo,
alberto.jimenez.diaz@urjc.es;
anegredo@fis.ucm.es

Citation:

Jiménez-Díaz, A., Negredo, A. M., Kirby, J. F., Sánchez-Pastor, P., Fullea, J., Ruiz, J., et al. (2023). The mechanical nature of the lithosphere beneath the Eastern Central Atlantic hotspots. *Geochemistry, Geophysics, Geosystems*, *24*, e2022GC010608. https://doi.org/10.1029/2022GC010608

Received 7 JUL 2022
Accepted 12 FEB 2023

Abstract

The Eastern Central Atlantic (ECA) region includes the Azores, Canary, Cape Verde, Great Meteor, and Madeira hotspots. These hotspots exhibit a large variety of characteristics and are rooted in the lithosphere ranging in age from newly created at the Mid Atlantic Ridge to Jurassic at the NW Africa Atlantic margin. Therefore, the ECA region represents an excellent scenario to investigate in an integrated way the effects of hotspots on the mechanical structure of oceanic lithosphere. Here, we calculate the effective elastic thickness (T_e) of the lithosphere from an analysis of gravity and topography. Azores hotspot is characterized by a $T_e < 10$ km, whereas the Great Meteor, Cape Verde, and Madeira hotspots have intermediate T_e (15–30 km) values. In contrast, the Canary hotspot is characterized by a much higher T_e (>50 km), forming the largest and most prominent mechanical feature in the ECA. All the hotspots except Canary show standard elastic thickness values when compared to average values for the same age lithosphere and to other oceanic areas in the world. The high strength of the Canary hotspot may be related to the highly depleted mantle composition in the area. The comparison between the elastic thickness distribution and the upper mantle seismic velocity structure shows no correlation between the T_e estimated at the ECA hotspots (with the exception of Azores) and the presence of low shear-wave velocity anomalies in the underlying mantle. This lack of correlation suggests a negligible effect of upper mantle temperature anomalies on the flexure of the ECA region.

Plain Language Summary

The upwelling of hot mantle material can modify drastically the thermal and mechanical properties of the rigid outer layer of the Earth (the lithosphere). In this study, we investigate the mechanical effects of the Azores, Canary, Cape Verde, Great Meteor, and Madeira hotspots on the oceanic lithosphere in the Eastern Central Atlantic. To do so, we use gravity and elevation data to analyze the spatial distribution of the effective elastic thickness of the lithosphere in this region, which is a proxy for the lithospheric strength. All of these hotspots except Canary show standard elastic thickness values when compared to the average thickness of the same age lithosphere. In contrast, the lithosphere in the Canary region is much stronger, and this high strength may be related to the nature of the underlying mantle. Finally, the presumed presence of hot mantle beneath these hotspots does not produce any weakening of the overlying lithosphere.

1. Introduction

The Eastern Central Atlantic (ECA) is characterized by the presence of a number of volcanic archipelagos, seamounts and plateaux, which are rooted in a crust ranging in age from 0 Ma at the Mid-Atlantic Ridge (MAR) to 180 Ma at the north-western African margin. The ECA includes five hotspots, namely, the Azores, Madeira, the Canary and Cape Verde archipelagos (often collectively termed as Macaronesia region), and the Great Meteor Seamount hotspot (Figure 1) that exhibit contrasting morphologic, geologic, and geophysical characteristics.

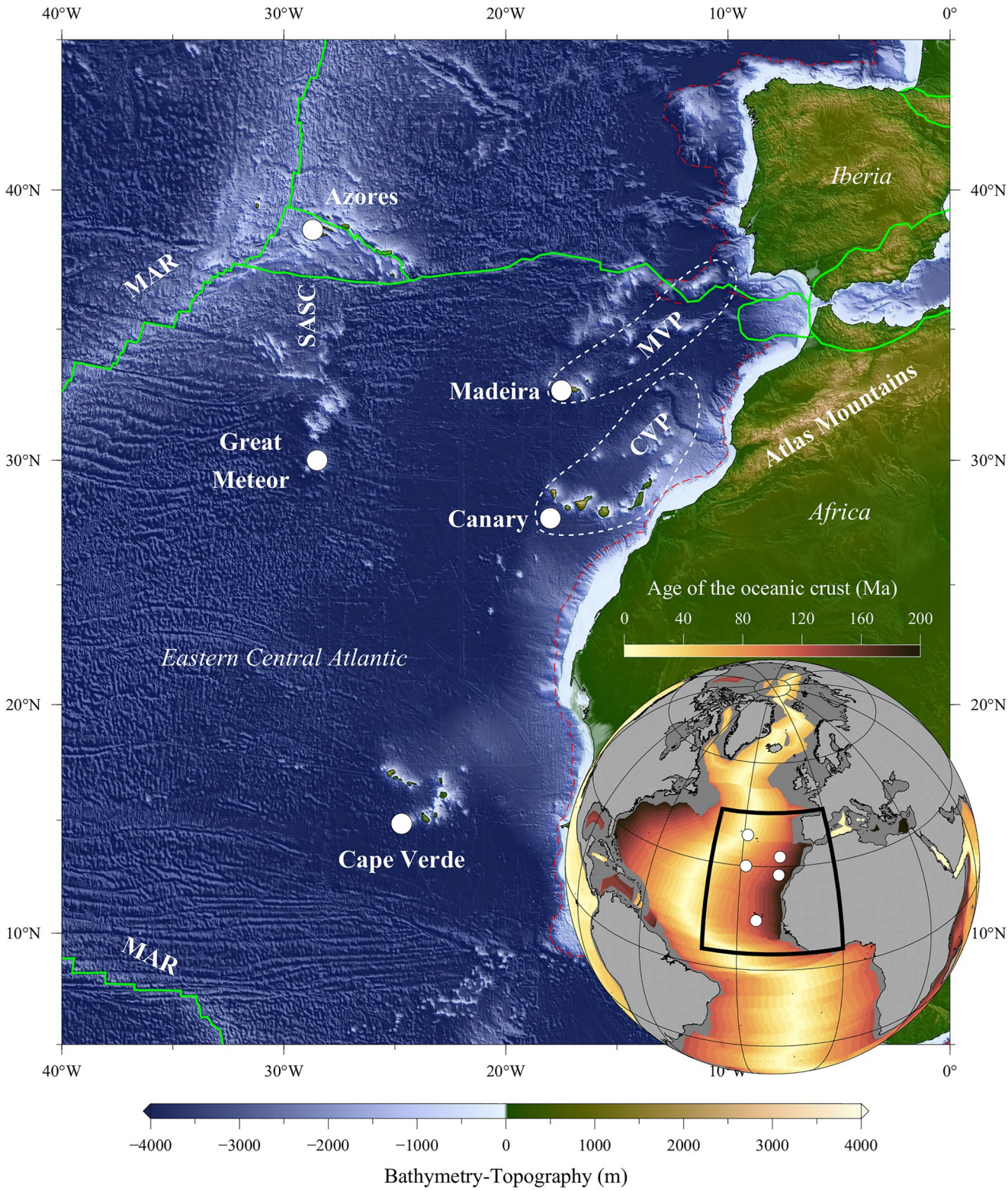

Figure 1. Topography and bathymetry of the Eastern Central Atlantic region (GEBCO_2022 Grid; GEBCO Compilation Group, 2022), showing seafloor age data (Seton et al., 2020) and plate and ocean–continent boundaries (green and red lines, respectively) from Hasterok et al. (2022) for context. The Madeira and Canary volcanic provinces are also shown bounded by white dashed lines (Geldmacher et al., 2005). Topography shaded relief superimposed. Abbreviations: CVP, Canary Volcanic Province; MAR, Mid-Atlantic Ridge; MVP, Madeira Volcanic Province; SASC, Southern Azores Seamount Chain; WAC, West African Craton. The five hotspots (white circles) are also labeled: Azores, Canary, Cape Verde, Great Meteor, and Madeira. The hotspot names and locations are from Jackson et al. (2021).

Therefore, ECA represents an excellent region for investigation of the mechanical effects of hotspots on the lithosphere and the mechanisms supporting intraplate oceanic chains in general.

A useful proxy used to characterize the long-term lithospheric strength is the effective elastic thickness (T_e). T_e corresponds to the thickness of an idealized purely elastic plate of homogeneous properties that would bend similarly to the actual lithosphere under the same applied loads (Watts, 2001), and is related to the integrated mechanical strength of the lithosphere (Burov & Diament, 1995; Watts & Burov, 2003). Previous studies have estimated T_e by means of different methods in different geological backgrounds. Such methods include direct measurements of flexure from seismic refraction data (e.g., Watts et al., 1985), stratigraphic data (e.g., Collier & Watts, 2001; Grotzinger & Royden, 1990), spectral analysis of the relationship between the topography/bathymetry and gravity (Bouguer or free air) or geoid anomaly (e.g., Audet, 2014; Kirby, 2014; McKenzie & Bowin, 1976) and thermo-rheological modeling of the lithospheric structure (e.g., Cloetingh et al., 2005; Tesauro et al., 2015). The variety of methods has led to different estimates of T_e even for the same areas, which makes it difficult to compare T_e results from different studies. This is the case of the five hotspots included in the study area. Furthermore, since many oceanic T_e studies have been restricted to particular geological features, the mechanical structure of most of the oceanic lithosphere in the study area remains unmapped, and therefore, the possible mechanical effects of hotspots are unknown.

In this work, we present the spatial variations of T_e in the ECA region from an analysis of the coherence between topography and Bouguer gravity anomaly using wavelet transforms. In order to gain a better insight into the possible origin of the hotspots in the area, we carried out a joint interpretation of the T_e distribution and the upper mantle seismic structure based on surface-wave tomography. In the following sections, we first describe key observations for the five hotspots included in the study area (Section 2). We then describe the methodology, data and parameters employed for estimating T_e (Section 3) and finally, we present the spatial variations of T_e (Section 4) and discuss the implications of our results (Section 5).

2. Geodynamic Setting

The Azores Plateau is characterized by a very broad bathymetric anomaly (about 1,000 km wide east-west; Figure 1) containing the triple junction between the North American, Eurasian and Nubian plates. Kinematic reconstructions from 35 Ma (chron 13) propose an age of 20 Ma for the initiation of the formation of the Azores plateau (Gente et al., 2003). The well-developed Azores swell and the presence of low S-wave velocities at 100–200 km depth (e.g., Zhang & Tanimoto, 1993) are consistent with a mantle plume origin for the plateau. However, the lack of any age progression (Feraud et al., 1980) has led to an alternative hypothesis proposing a shallower origin for the plateau related to plate boundary forces (Bonatti, 1990; Sartori et al., 1994).

The Great Meteor Seamount is rooted in a crust of 85 Ma age (Verhoef, 1984), and belongs to the Southern Azores Seamount Chain (SASC) located south of the Azores Plateau (Figure 1). The SASC is characterized by narrow isotopic variability that falls within the Azores isotopic field (Ribeiro et al., 2017). New K-Ar age determinations show nearly coeval volcanism along the chain, with ages of ~31–34 Ma (Ribeiro et al., 2017). A genetic link between the Azores Archipelago and the SASC has been proposed by Ribeiro et al. (2017) on the basis of geophysical observations (Gente et al., 2003) and recent geochemical and isotopic (Sr-Nd-Pb-Hf) data. These authors suggest that the geochemical similarity between the SASC and the Azores mantle source resulted from the long-lived (~85 Ma) Azores Plume.

Crude progression of increasing volcanic ages from southwest to northeast has long been recognized both in the Madeira and the Canary Volcanic Provinces (Abdel-Monen et al., 1972; Geldmacher et al., 2000, 2001; McDougall & Schmincke, 1976). The Madeira Province forms a ~700 km by ~200 km NE-SW-wide chain of volcanoes, with increasing ages from Madeira (0–5 Ma) to the Ormonde Seamount (65–67 Ma). The Canary Province is twice as wide E-W (~700 by ~400 km) and volcanic ages similarly range from 1.1 Ma at El Hierro (Guillou et al., 1996) to 68 Ma in the Lars Seamount (Geldmacher et al., 2001). This trend of increasing age to the northeast is further confirmed by the estimated oldest ages of shield stage volcanism in the seamounts in both provinces (Geldmacher et al., 2005). Although age progression is consistent with the conventional model of a hotspot created by a deep-seated and static mantle plume as first proposed for the Canary Province by Holik et al. (1991), this model neither explains the complex spatial and age distribution of volcanoes, nor the exceptionally long time interval (up to 40 Myr) of active volcanism at single volcanic centers. The cluster of seamounts

southwest of the Canary Islands have been recently dated (van den Bogaard, 2013) and found to be much older than the islands, with ages spatially scattered and ranging between 91 and 142 Ma. Given that these ages do not fit with the trend of increasing age to the northeast, the origin of these seamounts is commonly attributed to fracture-controlled volcanism, rather than to an upwelling mantle plume (van den Bogaard, 2013; Zaczek et al., 2015). The crudeness of the age progression of Madeira and Canary volcanic provinces is in contrast with the systematic and linear Hawaiian age progression derived from the ages of Hawaiian-Emperor seamounts (e.g., Duncan & Keller, 2004).

The Cape Verde Islands have been emplaced on the Early Cretaceous oceanic lithosphere of anomalously shallow bathymetry. The height and width of this swell are 2.2 and 1,200 km, respectively (Ali et al., 2003; Monnereau & Cazenave, 1990). There is no clear age progression of the islands, with estimated ages of about 8 Ma for the western islands and 10–20 Ma for the easternmost islands (Ali et al., 2003 and references therein). Despite the absence of a hotspot track, the hypothesis of an upwelling mantle plume is consistent with the elevated height of the bathymetric swell and with the velocity anomalies of several global and local seismic tomography studies (e.g., Boschi et al., 2007; Celli, Lebedev, Schaeffer, & Gaina, 2020; Celli, Lebedev, Schaeffer, Ravenna, & Gaina, 2020; Liu & Zhao, 2021; Montelli et al., 2006; Schaeffer & Lebedev, 2013; Zhao, 2007; see Section 5).

3. Method and Data

A useful proxy for the long-term lithospheric strength is given by the effective elastic thickness, T_e, which is related to the flexural rigidity, D, of a thin elastic plate by

$$D = ET_e^3/12\left(1-\nu^2\right) \quad (1)$$

where E is Young's modulus and ν is Poisson's ratio (e.g., Watts, 2001). To estimate T_e we calculate the coherence function relating the topography and Bouguer anomaly, commonly known as Bouguer coherence (e.g., Audet, 2014; Kirby, 2014), modeled with a simple thin elastic plate subject to both surface and subsurface loads. Specifically, we estimate the gravity and topography spectra, and thence their coherence, using the fan-wavelet transform (Kirby & Swain, 2004, 2011), which provides an observed coherence estimate at every point on the data grid. The wavelet transforms of the grids were computed using space domain convolution at the largest wavelet scales (longest wavelengths) and the Fourier transform at all others (Kirby & Swain, 2013). We use Morlet wavelet central wavenumber values of $|\mathbf{k}_0| = 2.668$ and 5.336, where the smallest value prioritizes the spatial resolution at the expense of wavenumber resolution, and vice versa for the largest value (Kirby & Swain, 2011).

The observed wavelet squared real coherency (SRC) is inverted for T_e using fan-wavelet adaptation of Forsyth's (1985) method (Kirby & Swain, 2008, 2009; Swain & Kirby, 2006). We follow Kirby and Swain (2009) and invert the SRC since it is less sensitive than the coherence to correlations between the initial loads on the plate and to the presence of topographically unexpressed internal loading (commonly known as "gravitational noise"), both of which can cause incorrect recovery of T_e (e.g., Audet & Bürgmann, 2011; Kirby, 2014; Kirby & Swain, 2009; McKenzie, 2003; McKenzie & Fairhead, 1997). In general, subsurface (internal) loads include mafic intrusions, accreted lower crustal material, thermal anomalies, and compositional variations, which cause lateral variations of density at depth, while surface loading is caused by topography and large-scale variations in surface density (e.g., mountains and sedimentary basins). Forsyth's (1985) method also yields the initial load ratio (f) between initial internal and surface loads, which we express here as an internal load fraction, F, where $F = f/(1+f)$ (McKenzie, 2003). Pure surface loading gives $F = 0$, purely internal loading gives $F = 1$, while equal surface and internal loading gives $F = 0.5$. We use Brent's method (Press et al., 1992) in the inversion to find the best-fitting predicted SRC, with the difference between observed and predicted SRCs weighted by the inverse of the equivalent Fourier wavenumber (Kirby & Swain, 2006). This inverse-wavenumber method generally gives smoother T_e maps than with computed errors, as it down-weights the noisy SRCs that sometimes occur at high wavenumbers. Errors on T_e are given as 95% confidence limits on the best-fitting value. For an extensive description of the method, see the Supplementary Material.

The bathymetry/topography data (Figure 1) used in our analysis are obtained from the GEBCO_2022 Grid, a continuous, global terrain model for ocean and land with a spatial resolution of 15 arc seconds (GEBCO Compilation Group, 2022). Although GEBCO 2022 uses SRTM15+ as a base, which contains altimetry-derived bathymetry, it is extensively supplemented with ship echo soundings, making it a much more quasi-independent dataset than bathymetry grids derived exclusively from altimetry estimates of the geoid. Therefore, the GEBCO

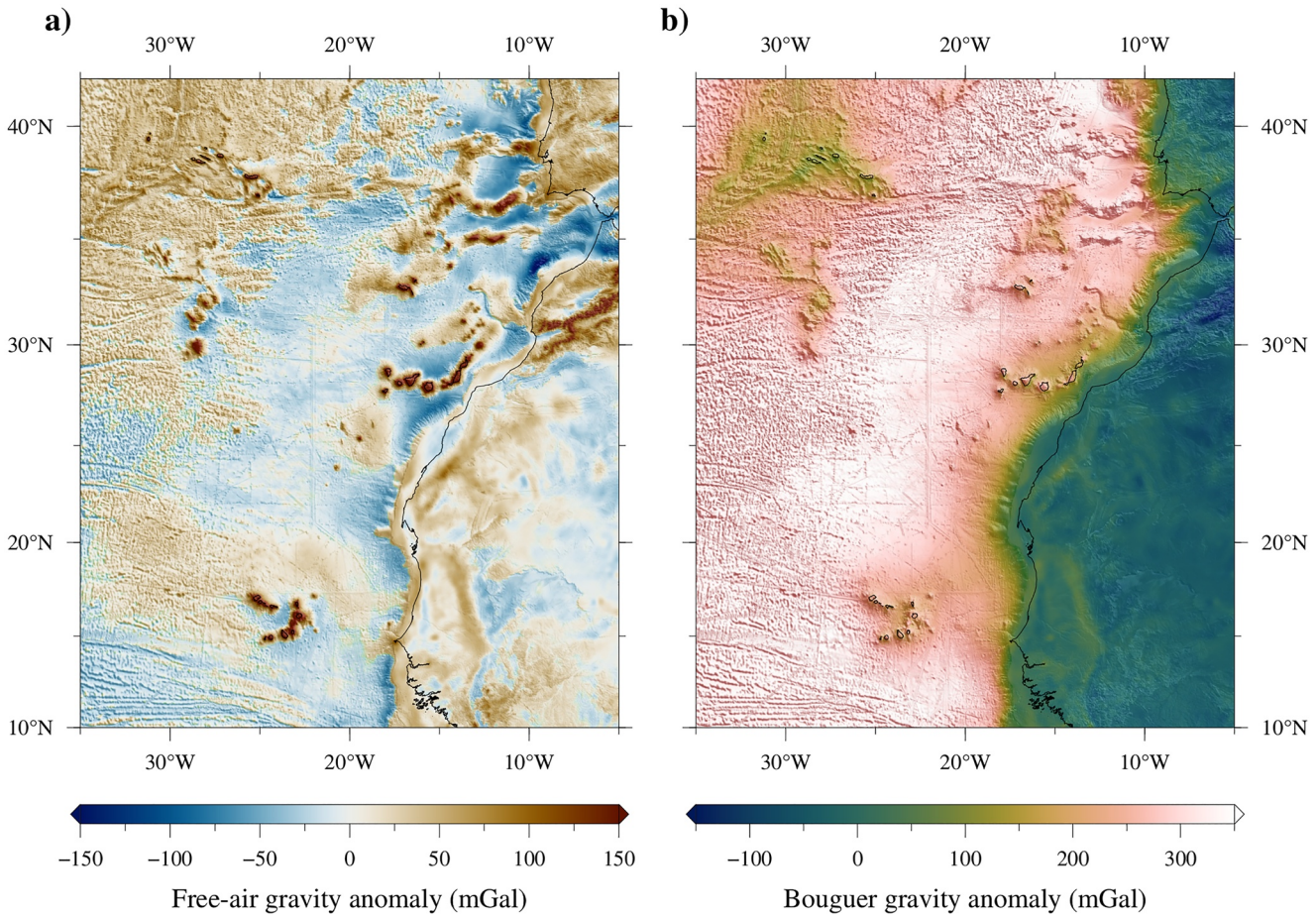

Figure 2. (a) Free-air and (b) Bouguer gravity anomalies used for the analysis (EGM2008 gravity model; Pavlis et al., 2008). Topography shaded relief superimposed.

bathymetry is preferred in T_e estimation over the oceans because it maximizes the independence of the gravity and bathymetry data sets (e.g., Kalnins & Watts, 2009; Lu et al., 2021). Our area contains both continental and oceanic lithosphere, with the latter being subject to an additional water load. To treat mixed land and marine environments, we adopt the approach of Stark et al. (2003) and Kirby and Swain (2008). This approach scales ocean bathymetry (h) to equivalent topography prior to Fourier transformation:

$$h_{\text{eq}} = h(\rho_{\text{uc}} - \rho_w)/\rho_{\text{uc}} \tag{2}$$

where ρ_w and ρ_{uc} are the seawater density (1,030 kg m^{-3}) and upper crust density (2,670 kg m^{-3}), respectively; that is, we scale the load of the ocean water to an equivalent topographic load. This allows the loading equations for a land environment to be used for the whole area, rather than performing two separate analyses and inversions on land and ocean areas, avoiding T_e discontinuities at the coastlines (e.g., Jiménez-Díaz et al., 2014; Pérez-Gussinyé et al., 2004; Ratheesh-Kumar & Xiao, 2018; Shi et al., 2017). For the purposes of comparison, T_e calculated using the regular bathymetry/topography is also presented in the Supplementary Material (Figures S1–S3 in Supporting Information S1). The Free-air and Bouguer gravity anomaly data over both land and ocean are obtained from the EGM2008 gravity model (Pavlis et al., 2008), with a spatial resolution of 2,5 arc minutes (Figure 2).

Sediments may play an important role in T_e estimation using spectral methods due to the significant density contrast with the underlying basement, which is not considered a priori (e.g., Chen et al., 2015; Ji et al., 2020; Kaban et al., 2018; Kirby, 2022; Ratheesh-Kumar et al., 2015; Shi et al., 2017; Yu et al., 2022). Large amount of sediments cause a flattening of the bathymetry and a prominent negative gravity anomaly, modifying the relationship between surface topography and gravity anomalies. Therefore, this combined effect of sediments can bias the T_e estimates based on the correlation between topography and gravity. Figure 3a shows the seafloor sediment thickness in the study area. The sediment thickness data are obtained from the GlobSed global model

10.1029/2022GC010608

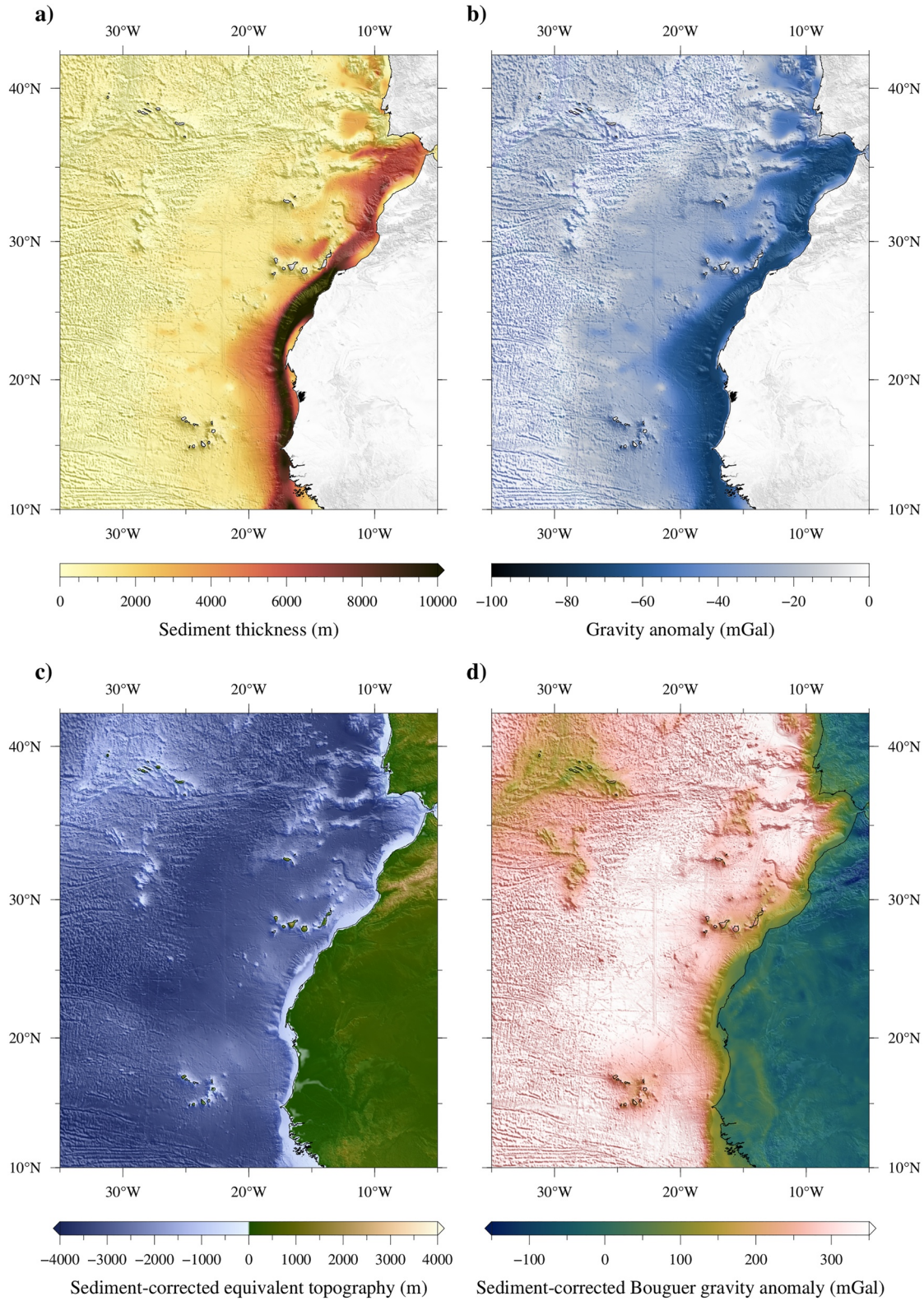

Figure 3. (a) Sediment thickness (GlobSed global model; Straume et al., 2019). (b) Gravity effect of sediments. (c) Sediment-corrected equivalent topography (derived from the GEBCO_2022 Grid; see the main text) and (d) sediment-corrected Bouguer gravity anomaly (derived from the EGM2008 gravity model) used for the analysis. Topography shaded relief superimposed.

(Straume et al., 2019), an updated total sediment thickness grid for the world's oceans and marginal seas with a spatial resolution of 5 arc minutes. Large amount of sediments are mainly located on the Gulf of Cadiz basin and offshore areas of western Iberia, and especially along the western continental margin of Africa where, in many cases, the sediment thickness exceeds 10 km. This can produce significant negative gravity anomalies reaching values of up to −80 mGal, as can be seen in Figure 3b.

Therefore, we examine the spatial variations of T_e in the study area considering sediments. We do so by using sediment-corrected bathymetry and gravity data sets. The gravity effect of sediments (Figure 3b) is calculated using the method of Rao and Babu (1991), and the sediment density model refers to the density-depth curves of offshore basins based on Mooney and Kaban (2010). The final Bouguer gravity anomaly is then calculated by subtracting the gravity effect of sediments from the complete Bouguer gravity anomaly. In addition, following the method of converting ocean bathymetry to equivalent topography (see above), the sediment thickness is also corrected, obtaining the final equivalent topography:

$$h_{\mathrm{eq}} = h(\rho_{\mathrm{uc}} - \rho_{w})/\rho_{\mathrm{uc}} + s(\rho_{s} - \rho_{\mathrm{uc}})/\rho_{\mathrm{uc}} \quad (3)$$

where ρ_w and ρ_{uc} are the seawater density (1,030 kg m^{-3}) and upper crust density (2,670 kg m^{-3}), and ρ_s and s are the sediment density and thickness, respectively; also scaled according to the sediment's density-depth curves (Mooney & Kaban, 2010). The sediment-corrected equivalent topography and Bouguer gravity anomaly are shown in Figure 3. To be clear, note that the flexural component of the sediment effect on bathymetry is not corrected for. The flexural effect of sediments depends on T_e, which is unknown a priori. We treat them as just another layer in the crust, and replace them with rock of mean crustal density (we actually account for a depth-dependent density; see above). It is, in essence just a Bouguer correction and an equivalent topography correction, but instead of replacing seawater with rock (or ice with rock), we replace sediments with rock, and work out the (a) change in gravity, and (b) the change in bathymetry. This correction considerably suppresses the effect of unexpressed subsurface loads and substantially reduces T_e estimates in areas where the topography variations are negligible and density variations within the sedimentary cover dominate (e.g., Kaban et al., 2018; Shi et al., 2017; Yu et al., 2022).

Forsyth (1985)'s method (often called “load deconvolution” as it seeks to recreate the initial loads from the final, post-flexure gravity and topography) requires estimates of crustal structure. Here, we assume a single-layered crust with internal loading occurring at the Moho, as did Forsyth (1985), and use the Moho depths and crustal densities provided by the global crustal model CRUST1.0 (Laske et al., 2013). Other constants used in the SRC inversion are the following: Newtonian gravitational constant, $G = 6.67259 \times 10^{-11}$ m^3 kg^{-1} s^{-2}; Young's modulus, $E = 100$ GPa; Poisson's ratio, $\nu = 0.25$; the gravity acceleration, $g = 9.79$ m s^{-2}; and mantle density, $\rho_m = 3{,}300$ kg m^{-3}.

We project all data sets to a Cartesian coordinate system using the Mercator projection in order to mitigate errors arising from the planar treatment of curvilinear coordinates. The study area has dimensions of 4,040 km (easting) × 4,570 km (northing), and a grid spacing of 10 km in both directions. The gravity/topography data are mirrored about their edges prior to Fourier transformation with the purpose of reducing spectral leakage, which in combination with the wavelet transform barely bias the results (see Kirby & Swain, 2008).

4. Results

The effective elastic thickness results for the two $|\mathbf{k}_0|$ values are shown in Figures 4–6. Low values of $|\mathbf{k}_0|$ provide better spatial resolution, while large values give a good resolution in the wave-number domain and a reasonably good resolution in the space domain. In this way, the results with different $|\mathbf{k}_0|$ can be interpreted as the result of applying different band-pass filters to T_e, bearing in mind that absolute T_e values are more reliable for higher $|\mathbf{k}_0|$ wavelets, while relative T_e differences are more faithfully represented by lower $|\mathbf{k}_0|$ wavelets (Kirby & Swain, 2011; Swain & Kirby, 2021). All of this can be seen in Figure 4, where the obtained T_e map with the $|\mathbf{k}_0| = 2.668$ shows a more detailed T_e structure, whereas T_e results from $|\mathbf{k}_0| = 5.336$ show a spatially smoother T_e pattern within the region. Thus, combining different $|\mathbf{k}_0|$ offers a comprehensive overview of T_e variations for the study area at different spatial scales.

For the purposes of comparison, Figures 4a and 4b show the sediment-uncorrected and the sediment-corrected T_e results estimated with $|\mathbf{k}_0| = 2.668$ and 5.336, respectively. In general, the Te results using the lowest $|\mathbf{k}_0|$ (2.668) wavelet remain similar, though the Canary Volcanic Province is characterized by a comparatively much

10.1029/2022GC010608

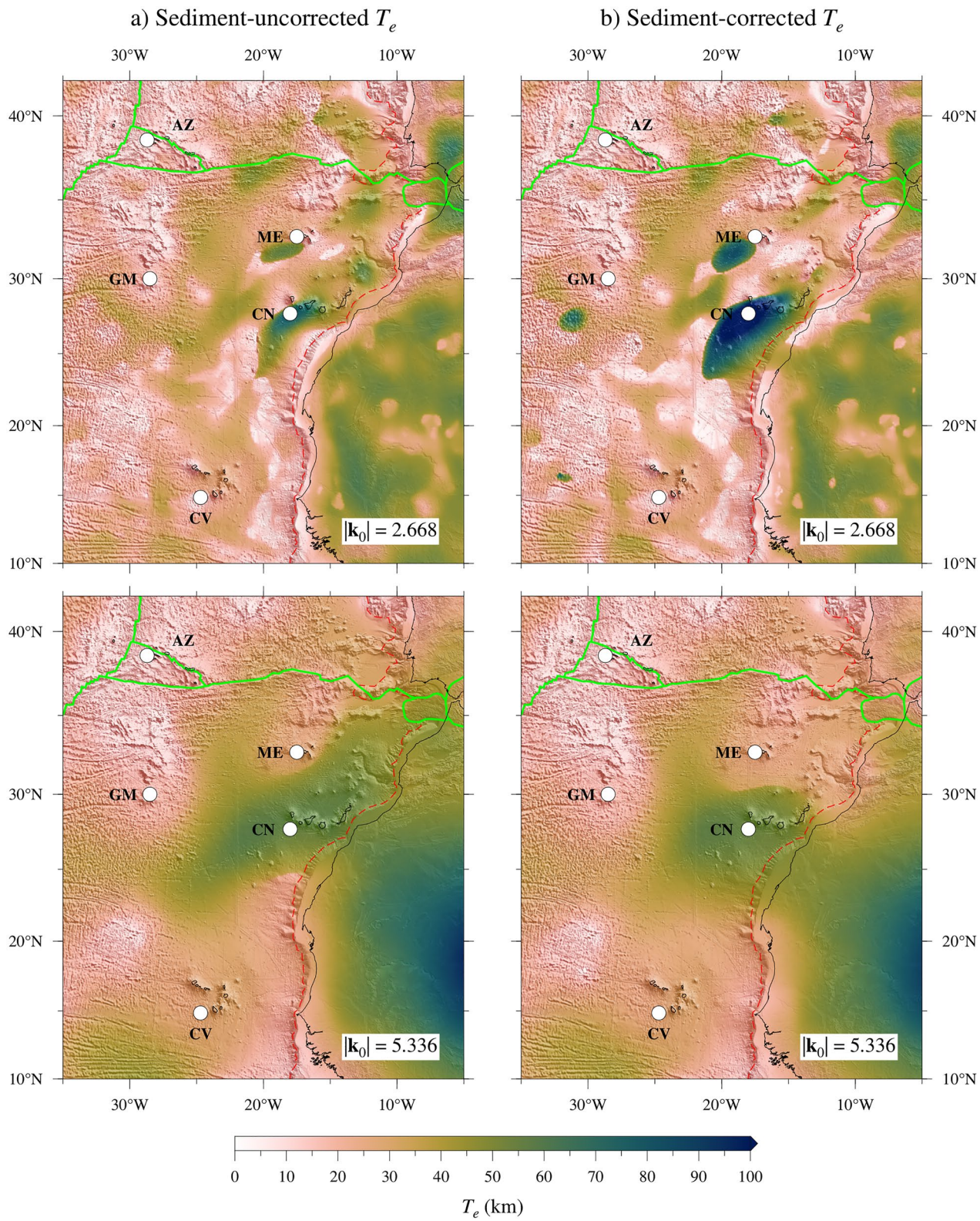

Figure 4. Effective elastic thickness, T_e, from the inversion of the squared-real Bouguer coherency using (a) the sediment-uncorrected and (b) the sediment-corrected equivalent topography and Bouguer gravity anomaly, with $|\mathbf{k}_0|$ = (a) 2.668 and (b) 5.336, respectively. Abbreviations: AZ, Azores; CN, Canary; CV, Cape Verde; GM, Great Meteor; ME, Madeira. The hotspot names, abbreviations, and locations are from Jackson et al. (2021).

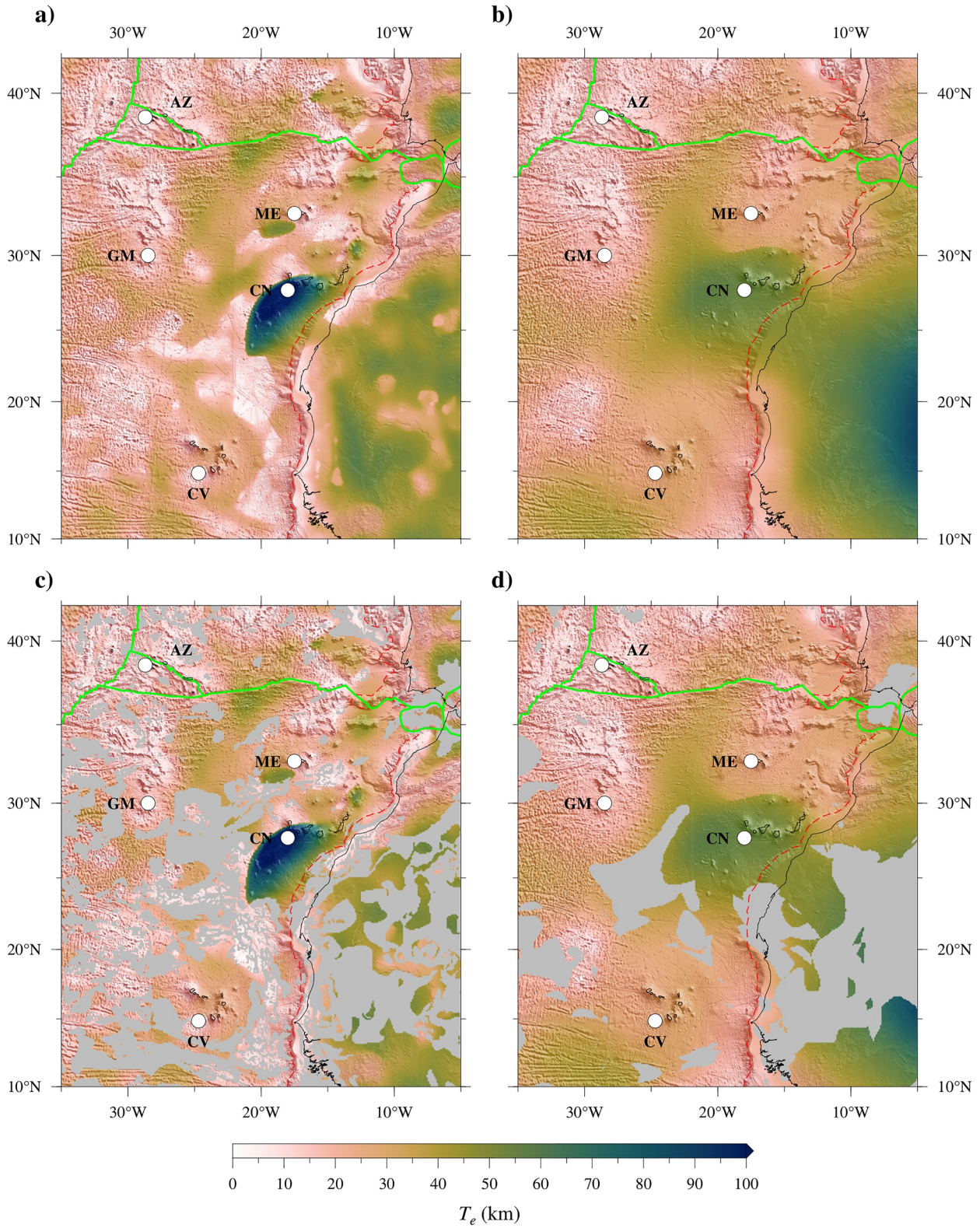

Figure 5. (a and b) Effective elastic thickness, T_e, from the inversion of the squared-real Bouguer coherency using the sediment-corrected equivalent topography and Bouguer gravity anomaly, for $|\mathbf{k}_0|$ = (a) 2.668 and (b) 5.336, respectively. (c and d) Effective elastic thickness, T_e, corresponding to the results in (a and b). Gray-shaded areas correspond to regions where T_e estimation might be biased by "gravitational noise." White circles indicate the locations where squared real coherency profiles ($|\mathbf{k}_0|$ = 5.336) are plotted in Figure 7. Abbreviations are the same as in Figure 4.

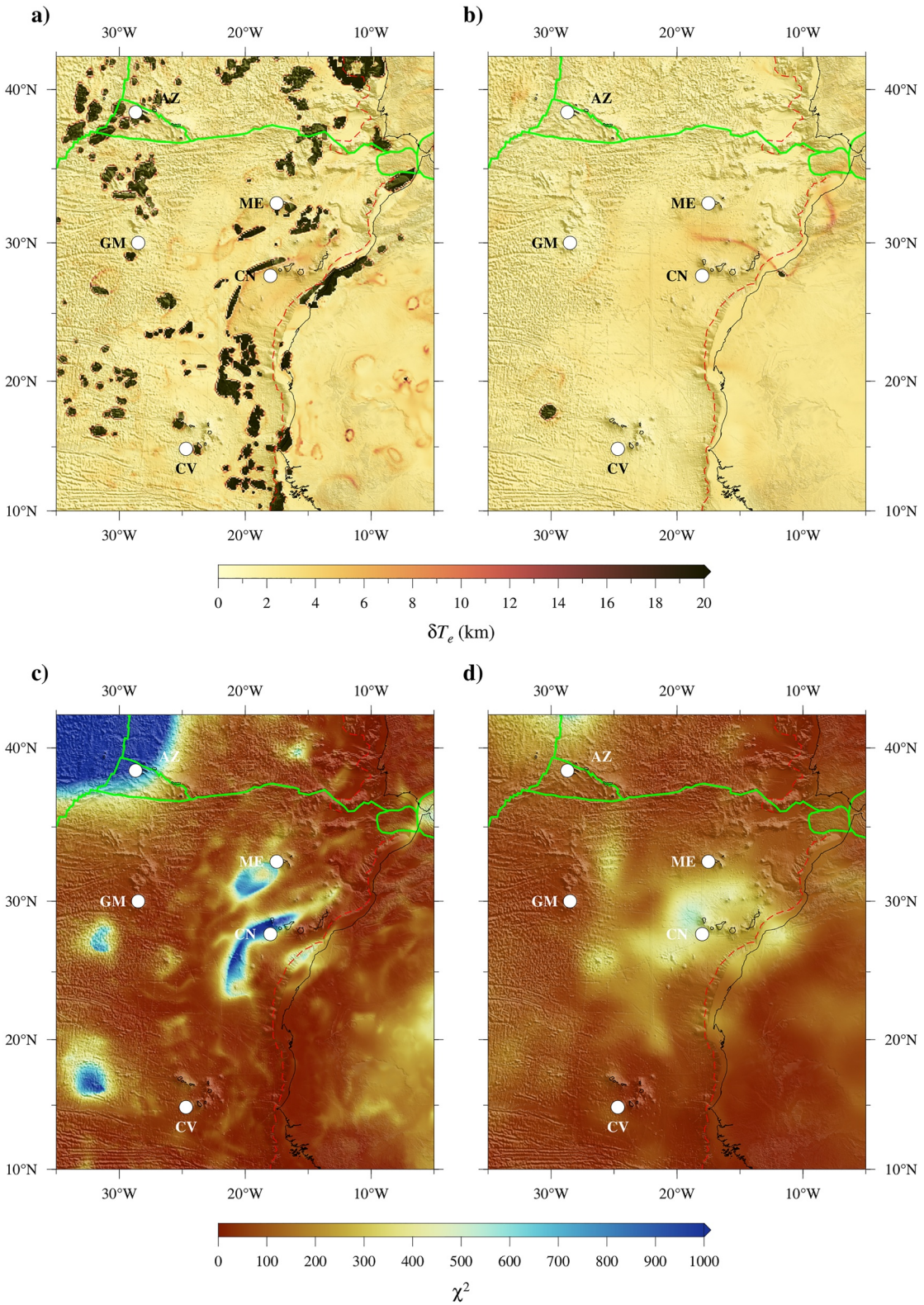

Figure 6. (a and b) T_e error and (c and d) chi-square misfit, corresponding to the T_e results in Figure 5, for $|\mathbf{k}_0|$ = (a) 2.668 and (b) 5.336, respectively. The color scale in (a) saturates at 20 km. Abbreviations are the same as in Figure 4.

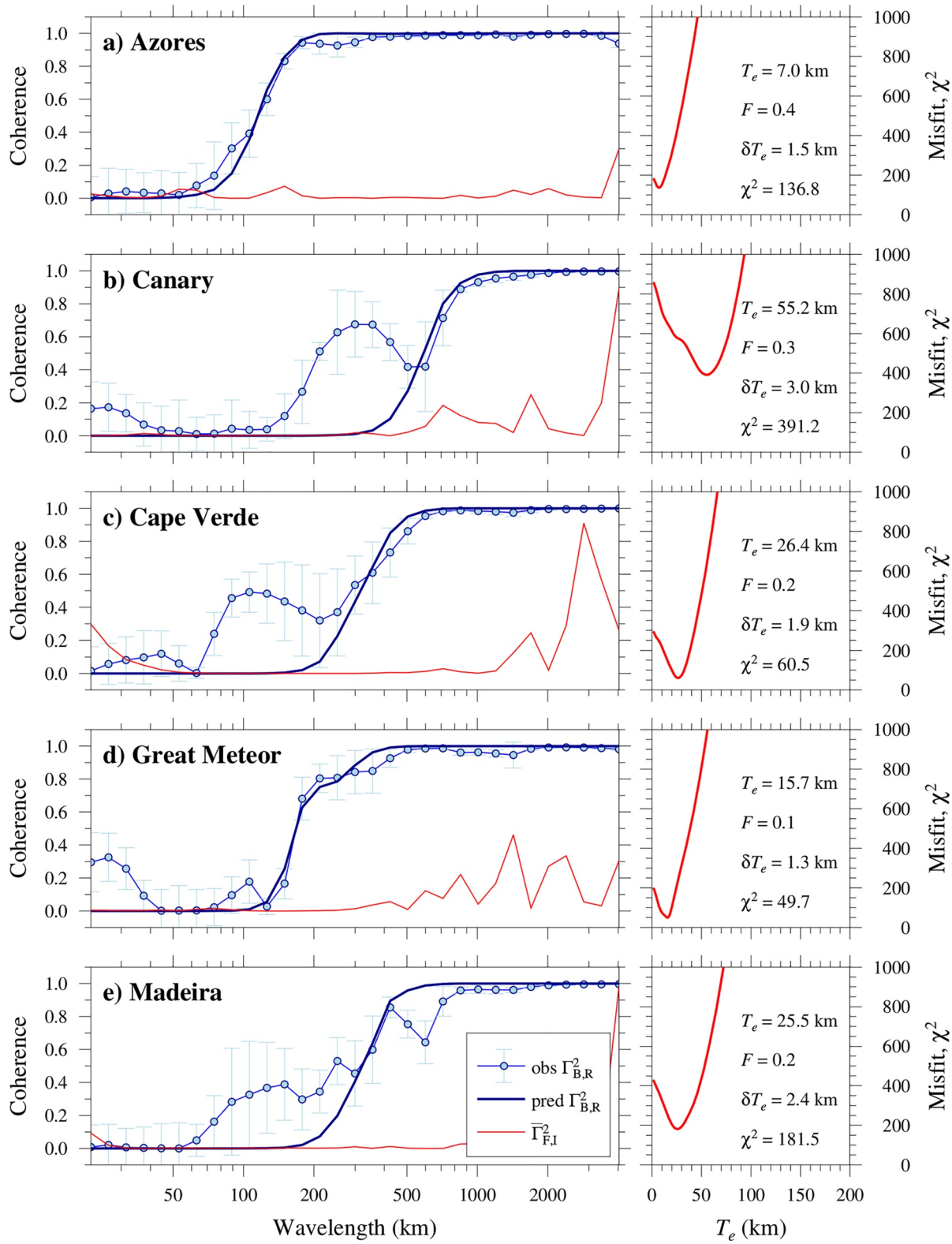

Figure 7. (a–e) Example of curve fitting and inversion results using the Bouguer squared real coherency (SRC) ($\Gamma^2_{B,R}$) for the five hotspots with $|\mathbf{k}_0|$ = 5.336. The autospectra and cross-spectra were averaged over spatial dimensions of 150 × 150 km and the observed coherency formed from these. Left panels: The observed Bouguer SRC (blue circles with their error bars and blue lines); the best-fitting predicted Bouguer SRC (dark blue lines); and the normalized free-air squared imaginary coherency, $\overline{\Gamma}^2_{F,I}$ (thin red lines). Right panels: misfit curves (thick red lines) used to estimate T_e using the Bouguer SRC; and the values of the best fitting T_e and F, as well as the value of the T_e error and chi-square misfit at all locations.

higher Te than previously observed in Figure 4a. In contrast, we note that the T_e results for $|\mathbf{k}_0| = 5.336$ show some important differences when considering the sediments. The most noticeable differences occur within the Gulf of Cadiz and the Madeira Volcanic Province, and along the northwestern continental margin of Africa, where the sediment-corrected T_e values are significantly smaller than the T_e results in Figure 4a, suggesting that the thick and less dense sediments have a large effect on the T_e results in these areas. Importantly, the presence of sediments does not significantly affect our T_e estimates for the hotspots in terms of absolute values (see for comparison Figure 7 and Figure S6 in Supporting Information S1). In the following section, we analyze our sediment-corrected T_e results in detail. Sediment-uncorrected results are also presented in Figures S4–S6 in Supporting Information S1.

Figure 5 shows the sediment-corrected T_e results with $|\mathbf{k}_0|$ = (a) 2.668 and (b) 5.336, respectively. Azores is characterized by a $T_e < 10$ km for both $|\mathbf{k}_0|$ values. The Great Meteor and Cape Verde show a slightly higher T_e value of 15–30 km, both being bounded by higher T_e values (especially noticeable with the lowest $|\mathbf{k}_0|$ value; see Figure 5a). The Madeira and Canary volcanic provinces are characterized by a complex pattern of T_e. The Madeira Islands exhibit a T_e of 15–30 km for both $|\mathbf{k}_0|$ values. However, for $|\mathbf{k}_0| = 2.668$, this T_e pattern over the Madeira Islands shows a moderate increase along the northeastern Madeira Volcanic Province, and an abrupt increase in T_e along the southwest of the Madeira Islands (Figure 5a). Finally, the Canary Islands are characterized by T_e values exceeding 50 km. This T_e pattern also extends to the west and southwest of the Canary Islands (with a steep gradient with the lowest $|\mathbf{k}_0|$ value; see Figure 5a), forming the largest, and highest in terms of T_e, feature in the Eastern Central Atlantic. We note that T_e results for $|\mathbf{k}_0| = 5.336$ appear to be more influenced by the high values recovered over Africa, where the high T_e of the West African Craton has been extended westwards (due to the comparatively lower spatial resolution of such wavelets).

We analyze the bias in T_e estimation related to the effect of gravitational noise following the approach of Kirby and Swain (2009), based on the normalized free-air squared imaginary coherency (SIC). Figures 5c and 5d show the effective elastic thickness, T_e, from the inversion of the squared-real Bouguer coherency ("Bouguer SRC") with $|\mathbf{k}_0|$ = (a) 2.668 and (b) 5.336, respectively. Gray-shaded areas correspond to regions where T_e estimation might be biased by noise based on our analysis (i.e., regions where the maximum value of the normalized free-air SIC exceeds 0.5). Note that while large noise indicates a potential failure of the load deconvolution method, it does not imply that the lithosphere is weak (Audet & Bürgmann, 2011). Kirby and Swain (2011) found that the size of the affected area increases as $|\mathbf{k}_0|$ decreases (see Figures 5c and 5d), and also that the lower wavenumber resolution of low-$|\mathbf{k}_0|$ wavelet results in the noise spectrum being smeared over a larger bandwidth than with high-$|\mathbf{k}_0|$ wavelets. In this regard, we note that noise does exist in the study area. However, the five hotspots are either slightly affected (Azores and Great Meteor; see Figure 5) or even unaffected, especially when using the highest $|\mathbf{k}_0|$ value.

Figure 6 shows T_e error and the spatial variation of the chi-square statistic minimized in the inversion of the Bouguer SRC ($|\mathbf{k}_0| = 2.668$ and 5.336), corresponding to the T_e results in Figure 5. We limit the color scale to a maximum T_e error of 20 km. Uncertainty for T_e estimates is low, although higher errors (with a maximum T_e error >100 km) are found in some areas surrounding the five hotspots in the lowest $|\mathbf{k}_0|$ results (Figure 6a). We note that the chi-square misfit can be quite high in some regions, especially when using the lowest $|\mathbf{k}_0|$ (Figure 6c). Note that Figures 6c and 6d provide a measure of how well the observed and best-fitting predicted SRC fit. Therefore, Figures 6c and 6d contain qualitative information about T_e errors and show regions where the model may be inappropriate and/or the data errors have been underestimated. We find the highest values in the northwest of the Azores Plateau. Other areas with very high chi-square misfit values coincide with the higher T_e along the southwest of the Madeira Islands (see Figure 5a), and a narrower band along the southwest of the Canary Islands, which likely reflects an overestimation in these areas.

Finally, as an additional test of the robustness of the inversion and T_e estimates, Figure 7 shows the results of inverting wavelet SRC profiles for the five hotspots with $|\mathbf{k}_0| = 5.336$, hence prioritizing absolute T_e values. Rather than computing the coherency at each of the 10 × 10 km grid nodes, we spatially averaged the auto-spectra and cross-spectra over 15 × 15 grid nodes, giving a 150 × 150 km spatially averaged coherency. The thin red lines show the normalized squared imaginary component of the free-air coherency. Large values at wavelengths just less than the transition wavelength (from low to high Bouguer SRC) indicate a T_e estimate likely biased by gravitational noise. High values of the normalized free-air SIC occur at wavelengths that do not affect the SRC rollover in these regions (Figure 7). Furthermore, the chi-square misfits are all very narrow with well-defined minima, indicating that the recovered T_e values are robust. However, we note that Canary and Cape Verde present a

complex pattern with two rollovers, suggesting two dominant T_e values (see also Figures S3 and S6 in Supporting Information S1). For Canary, the longer-wavelength rollover at 600–700 km wavelength provides the estimation. If we consider the shorter-wavelength rollover at ∼200 km wavelength, a lower T_e would be plausible. The long, shallow-gradient rollover in Madeira also suggests a wide range of T_e values, possibly similar to Canary and Cape Verde. These results suggest the support of different loads that may be operating at small- and large-scales simultaneously, or even at different times, in these regions. In this regard, it is worth noting that the volcanic activity is very long lasting, particularly in the Canary volcanic province, and therefore the lithosphere was loaded at different times. For example, small seamounts to the south of El Hierro have volcanic ages as old as 140 Ma (van den Bogaard, 2013), so they were emplaced in much younger lithosphere, which could have responded in a very different way from the Jurassic lithosphere at the time of the formation of the Canary Islands (subaerial volcanic ages 23-1 Ma). We will return to this issue in Section 5.4.

5. Discussion

5.1. Comparison With Previous T_e Estimates

The values obtained for T_e are, in general, in good agreement with previous estimates for the different analyzed regions, except for the Canary Volcanic Province. The present study predicts a T_e value for the Azores Archipelago and SASC areas as low as 5–7 km, in good agreement with the T_e of 3 ± 3 km obtained by Calmant et al. (1990), and of 3–6 km obtained by Luis and Neves (2006) from 3D admittance and coherence study. The obtained T_e for Great Meteor (∼16 km) is consistent with the values of around 20 km obtained by Watts et al. (1975) and Calmant et al. (1990). Similarly, taking into account the uncertainties, our results for Cape Verde (24–28 km) and Madeira (23–28 km) are comparable to previously reported values of, respectively, 12–35 km (Ali et al., 2003; Calmant et al., 1990; Kalnins, 2011; McNutt, 1988; Young & Hill, 1986) and 15–35 km (Calmant et al., 1990; Kalnins, 2011).

In contrast, the T_e values derived here (>50 km) for Canary are at least 10–35 km higher than the range of 15–40 km obtained from several previous works (Canales & Dañobeitia, 1998; Collier & Watts, 2001; Dañobeitia et al., 1994; Kalnins, 2011; Llanes, 2006; Watts, 1994; Watts et al., 1997), but similar to the ∼50 km estimates by Filmer and McNutt (1989) and consistent with the T_e maps obtained by Pérez-Gussinyé et al. (2009) and Audet and Bürgmann (2011). The flexural analysis of the static elevation residuals by Fullea et al. (2015) also suggested a mechanically strong lithosphere, in line with the normal thermal lithospheric thicknesses of 110 ± 20 km obtained in their study. This is consistent with the presence of a relatively small amplitude swell (Canales & Dañobeitia, 1998) and the absence of long-wavelength gravity and geoid anomaly centered in the Canary Islands (Fullea et al., 2015; Watts, 1994). We will return to this issue in Section 5.4.

5.2. Relationship Between T_e and the Temperature of the Oceanic Lithosphere

The usual way of systematizing the relation between the mechanical and thermal states of the oceanic lithosphere is to compare T_e and the age of the lithosphere at the time of loading (i.e., the difference between the age of the lithosphere and the age of the load), with the depth to specific isotherms. Based on that, several works have found a general correlation between T_e and the depth to the 300–600°C isotherms (e.g., Watts, 2001).

Figure 8a shows the relationship between T_e and the age of the oceanic lithosphere for the five hotspots studied in this work (T_e results using $|\mathbf{k}_0| = 5.336$; see Figure 7 and Table 1). The isotherm distribution corresponds to the cooling-plate model of Parsons and Sclater (1977). For the purposes of comparison, the thick black line represents the mean T_e estimates for the same age from the gridded T_e results using $|\mathbf{k}_0| = 5.336$ (Figure 5), versus the age of the oceanic crust from Seton et al. (2020). There is a systematic increase in T_e with plate age for lithospheres younger than 130 Ma, consistent with models for the cooling of oceanic lithosphere as it moves away from a mid-ocean ridge and the temperature-dependent ductile creep of lithospheric minerals such as olivine (e.g., Hunter & Watts, 2016). For older lithospheres, T_e remains nearly constant or even decreases with plate age from 34 to 28 km. Low T_e values (compared to expected values for very old lithosphere) are found along most passive continental margins. The reason why passive margins tend to be relatively weak remains an open question, with some authors invoking thermal and fluid-related effects in rifting processes (e.g., Audet & Bürgmann, 2011; Pérez-Gussinyé et al., 2009; Ratheesh-Kumar & Xiao, 2018) or accumulated weakening of the passive margins caused by grain damage (Mulyukova & Bercovici, 2018). In turn, Bercovici and Mulyukova (2021) have shown that combined grain damage and mixing enlarges the range of temperatures and depths for the occurrence of this

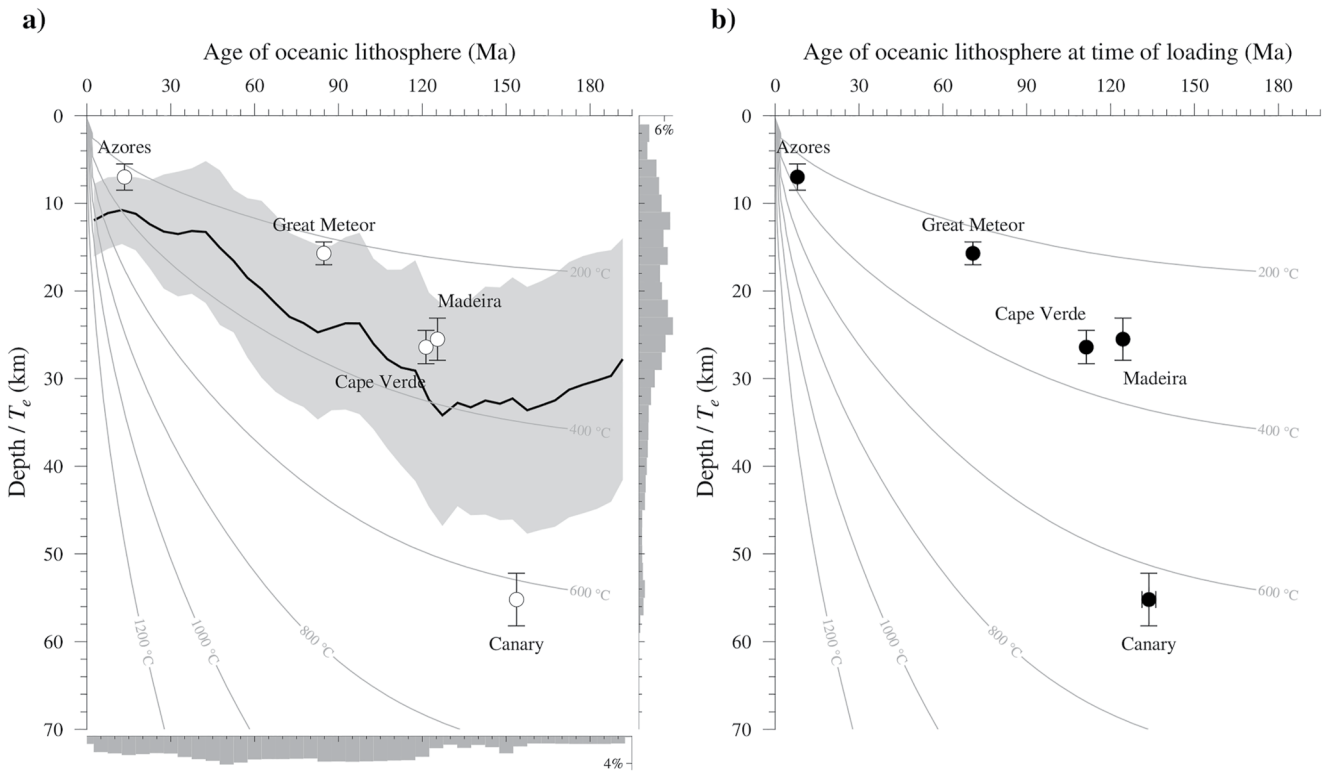

Figure 8. (a) T_e estimates for the five hotspots versus the age of the oceanic lithosphere. Thick black line represents the mean T_e estimates (± the standard deviation about the mean; gray envelope) from the gridded T_e results using $|\mathbf{k}_0| = 5.336$ (Figure 5b), versus the age of the oceanic crust from Seton et al. (2020). The gray curves show the depth to the plate-cooling isotherms of Parsons and Sclater (1977). (b) T_e estimates for the five hotspots versus the age of the oceanic lithosphere at the time of loading (see Table 1).

weakening. The average T_e obtained for the ECA region roughly follows the depth of the 350–400°C isotherms, with an envelope of approximately 200–500°C (described by the standard deviation band).

Figure 8b shows the relationship between T_e and the age of the lithosphere at the time of loading. Although the age of the lithosphere was similar when it was loaded at Canary, Cape Verde and Madeira areas, the T_e results are very variable, implying a correlation with isotherms depths expanding by roughly a factor two (taking into account uncertainties). The T_e for Canary roughly correlates with the depth to the isotherm of 640 ± 40°C, whereas T_e for Cape Verde and Madeira correlates with the depth to the isotherm of 340 ± 30°C and of 310 ± 40°C, respectively. The T_e for Azores correlates with the depth to the isotherm of 340 ± 80°C, and the T_e obtained for the lithosphere loaded by the Great Meteor seamount correlates with the depth to an isotherm of 250 ± 30°C.

Table 1
Summary of the Estimates of Elastic Thickness, T_e

	Age of seafloor (Ma)[a]	Age of load (Ma)	Load age error (Myr)	T_e (km)[b]	T_e error (km)[b]
Azores	13.47	5.5[c]	-	7.0	1.5
Canary	153.68	20[d]	2.5[d]	55.2	3.0
Cape Verde	121.31	10[e]	0[e]	26.4	1.9
Great Meteor	84.76	14[e]	0[e]	15.7	1.3
Madeira	125.41	1[e]	0[e]	25.5	2.4

[a]Age of the oceanic crust from Seton et al. (2020). [b]T_e and T_e error from the results of inverting wavelet squared-coherency profiles ($|\mathbf{k}_0| = 5.336$) for the five hotspots (see Figure 7). [c]Based on Feraud et al. (1980). [d]Dañobeitia et al. (1994). [e]Calmant et al. (1990).

The T_e value for the Great Meteor can be considered as relatively low when compared with the average value for the lithosphere of the same age in the ECA region, although it falls within the standard deviation band (Figure 8a). The correlating isotherm of 250 ± 30°C is slightly colder than the envelope of 300°C–600°C found in the extensive compilation by Watts and Zhong (2000), but it is still within the range of values for a number of seamounts and volcanic islands computed in more recent studies (Kalnins & Watts, 2009; Watts et al., 2006). For example, Watts et al. (2006) compared the predicted bathymetry to shipboard bathymetry measurements and obtained >9,000 T_e estimates from a broad range of submarine features in the Pacific, Indian, and Atlantic oceans included in the Wessel (2001) global seamount database. They found that many T_e estimates plotted outside the expected 300–600°C isotherm depth range. A re-assessment by Kalnins and Watts (2009) in the area of the Western Pacific Ocean found that bathymetric features formed on the Jurassic seafloor have an envelope of 50–300°C, with a best fit of

180°C. Similarly, the recent study by Lu et al. (2021) found that 80% of their T_e estimates over the Pacific basin correspond to depths of a broad range of isotherms, with envelopes of 220 ± 195°C and 270 ± 210°C based on two different cooling plate models. Although the present study further supports that there is no single isotherm that describes all the T_e data even for the same region (wide standard deviation in Figure 8a), four of the five hotspots analyzed plot within the 250–350°C isotherm, in line with the above-mentioned studies. In contrast, the well-studied Hawaiian chain has a T_e value of 30–35 km (Watts, 1978; Zhong & Watts, 2013), which correlates with the warmer 450 ± 150°C isotherm for a lithospheric age at the time of loading of 70–80 Ma. Overall, the only clearly anomalous T_e value is the one estimated for the Canary province, with a value >50 km correlating with the ~650°C isotherm. This correlation with deep geotherms is found only in oceanic trenches (e.g., Levitt & Sandwell, 1995; McAdoo & Martin, 1984), fracture zones in the Pacific (T_e described by the depth to the 600°–700°C isotherms; Wessel & Haxby, 1990) and the New England seamounts (T_e correlated with an isotherm in the range of 750–850°C; Zheng & Arkani-Hamed, 2002).

Watts et al. (2006) tentatively assigned a tectonic setting to each T_e estimate. They assigned seamounts in the range $0 < T_e < 12$ km an ''on-ridge'' setting, seamounts with intermediate estimates $12 < T_e < 20$ km a "flank ridge" setting, and seamounts with $T_e > 20$ km an "off-ridge" setting. Considering the T_e estimates for the five hotspots analyzed in the present study, this classification is consistent with the "on ridge" setting of Azores, "flank ridge" of Great Meteor, and "off ridge setting" of Cape Verde, Madeira and Canary hotspots.

5.3. Comparison With Seismic Structure of the Upper Mantle

Compared to previous studies focused on specific areas, the regional approach adopted here enables a direct comparison between the lithospheric strength and the seismic structure of the lithosphere and upper mantle. Figure 9 shows the shear-wave velocity anomalies at different depths in the upper mantle from the surface-wave tomography model SA2019 (Celli, Lebedev, Schaeffer, Ravenna, & Gaina, 2020). At shallow depths (above 80 km), all the hotspots except Azores show high seismic velocities (bluish colors). At larger depths, all the hotspots show slow velocity values (reddish colors), with Azores and Cape Verde being slower than Canary, and Madeira being located at the periphery of the Canary anomaly. At 200 km depth, the negative velocity anomaly beneath Azores starts vanishing and Cape Verde exhibits the most negative anomaly. At 330 km, Azores presents a strong positive anomaly, Canary/Madeira neutral to slightly positive and the velocity model below Cape Verde remains negative. On the basis of the interpretation of these anomalies as temperature-derived, Azores is a "shallow" (source depth <200 km) hotspot on top of a ridge, while Cape Verde is a "deep" hotspot characterized by a negative velocity anomaly in most of the upper mantle.

The comparison between Figures 5 and 9 reveals that, except for Azores, there is no correlation between the T_e estimated at the ECA hotspots and the amplitude of low shear-wave velocity anomalies in the underlying mantle. If the mechanical thickness of the hotspot were controlled by the presence of anomalously warm upper mantle material (on the basis of the interpretation of temperature-related seismic anomalies), one should expect similar T_e values for Cape Verde and Canary (possibly lower in Cape Verde) and a higher T_e in Madeira. Instead, our results show similar T_e values for Cape Verde and Madeira (Figures 5 and 8), and much higher T_e values beneath the Canary region. This lack of correlation between the elastic thickness and upper mantle temperature is in agreement with recent convection simulations of plume-lithosphere interaction at the Hawaiian Islands by Bellas et al. (2020), who showed that thermal erosion from a plume only perturbs the deepest part of the lithosphere, while the rest of the plate remains strong. The recent convection modeling of the interaction between an upper mantle plume and the lithosphere beneath the Canary Islands region by Negredo et al. (2022) is also consistent with an almost negligible thermal erosion or viscosity reduction caused by the highly mobile mantle plume. The joint interpretation of the T_e and the seismic velocity structure performed in the present study permits extending this inference of the negligible effect of upper mantle temperature anomalies on the flexure to the ECA region.

5.4. On the Strength of the Lithosphere in the Canary Islands Region

Our results indicate the standard elastic thickness of the oceanic lithosphere beneath the ECA hotspots. However, the Canary hotspot is the notable exception, with a complex pattern of T_e. Our T_e results over the Canary Islands region are the highest values for intraplate volcanic islands worldwide (see e.g., Watts, 2001; Watts et al., 2006; Watts & Zhong, 2000); similar oceanic $T_e > 50$ km values are found only along some trenches (e.g., Hunter & Watts, 2016; Levitt & Sandwell, 1995; McAdoo & Martin, 1984; Yang & Fu. 2018). The very high strength of the lithosphere at the Canary hotspot is apparently in contrast with the prominent negative shear-wave velocity

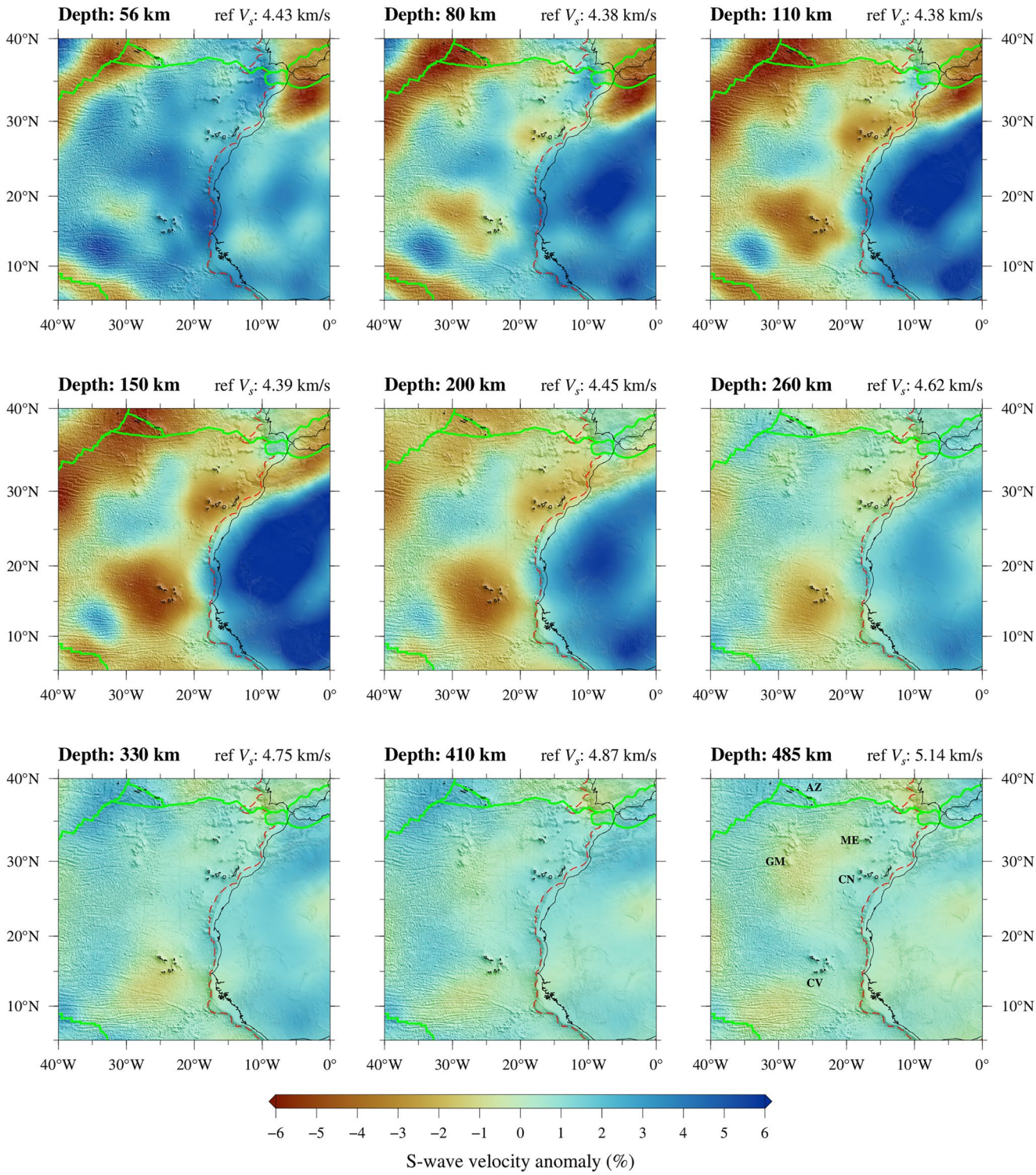

Figure 9. Seismic shear wave velocity anomaly at different depths in the lithosphere and upper mantle from the tomography model SA2019 (Celli, Lebedev, Schaeffer, Ravenna, & Gaina, 2020). Abbreviations are the same as in Figure 4.

anomaly down to 200 km (Figure 9). Fullea et al. (2015) suggested a sublithospheric temperature anomaly of 100 K on the basis of integrated geophysical and petrologic modeling. However, these authors did not find a significant thermal thinning or mechanical weakening of the lithosphere that could be related to the anomalously hot sublithospheric mantle. The convection modeling by Negredo et al. (2022) also showed negligible thermal

erosion of the lithosphere beneath the Canary region. This absence of weakening is in agreement with the high T_e estimates independently derived by the present work.

On the other hand, we note that the high T_e over the Canary Islands region is the most major discrepancy between this and previous studies, which yield T_e values ranging between 15 and 40 km (Canales & Dañobeitia, 1998; Collier & Watts, 2001; Dañobeitia et al., 1994; Kalnins, 2011; Llanes, 2006; Watts, 1994; Watts et al., 1997). These differences can be attributed to the use of different approaches and methods, different values of parameters, and/or different sizes of the study area. Focusing on the spectral estimates of T_e, it is important to note that the wavelet method provides a coherence estimate at every point on the data grid (see above). This allows us to map out the spatial variations in T_e over the Canary region instead of obtaining a single estimate of T_e within a finite-size window, representative for the entire analyzed area. To evaluate this effect, we calculated the spatial variations in T_e over the Canary region in the same way as in our main results as well as averaging over the entire area (see Figure S8 in Supporting Information S1). The coherence calculated averaging over the entire area yields a T_e value of 26.7 $\pm$ 2.8 km for the Canary region, which is in good agreement with previous estimates.

A factor that can be related to the extremely high values of T_e in the Canary Islands region (Figure 5) is the presence of chemically depleted (therefore dry and more viscous) lithospheric mantle material (Neumann et al., 1995, 2002; Wulff-Pedersen et al., 1996). The lithospheric mantle xenoliths from the Canary Islands show ultra-refractory compositions that have been interpreted as residues after partial melting beyond the stability of primary clinopyroxene (Simon et al., 2008). Whether this hypothetical compositional strengthening can be applied to other hotspots or not needs further investigation. For example, Ito et al. (1999) obtained a significant viscosity increase due to water extraction from the mantle due to partial melting of the Iceland mantle plume.

The particular mechanical signature of the Canary Islands region could be affected by its close location to the edge of the West African Craton (Figure 9), and the possibility of the occurrence of edge-driven convection (EDC). This mechanism would generate small-scale convection caused by the contrast between thick cratonic lithosphere and normal or thin lithosphere and has been suggested by King and Ritsema (2000) as the origin of African plate hotspot volcanism. Numerical modeling of EDC in the Atlas Mountains by Kaislaniemi and van Hunen (2014) shows that the upwelling mantle in the convection cell makes decompression melting possible. After melt removal, a layer of dry and depleted material is left behind. This viscous (drier) and buoyant layer tends to stick to the base of the lithosphere, possibly increasing its strength. Recent numerical modeling efforts consistently find that the EDC mechanism is not consistent with the extent of a melting anomaly beneath the Canary Archipelago (Negredo et al., 2022) or even with the melting occurrence itself (Manjón-Córdoba Cabeza & Ballmer, 2021). Negredo et al. (2022) found that the interplay between an upper mantle thermal plume and the strongly heterogeneous lithosphere results in an asymmetric mantle flow and in lateral migration (away from the craton edge) of the plume head, in agreement with the overall westward decrease in the age of the islands. In turn, this laterally migrating pattern would prevent effective thermal weakening in the overlying lithosphere and T_e reduction.

As indicated by the complex SRC pattern with two rollovers (Figure 7), a lower T_e value would also be plausible. The complex T_e pattern can be understood in terms of the very wide range of volcanic ages in the Canary volcanic province. For example, the Bisabuelas (Grand-grandmothers, as termed by van den Bogaard, 2013) a small group of seamounts located 70 km southwest of El Hierro has ages up to 142 Ma, in contrast with the <1.1 Ma age of El Hierro island. Actually, van den Bogaard (2013) nominated the Canary Island Seamount Province as the most long-lived hotspot preserved on earth. We hypothesize that lower T_e values are likely reflecting load compensation of small seamounts located to the southwest of the archipelago, which show ages varying from 142 to 91 Ma (van den Bogaard, 2013) and therefore erupted in a much younger (<60 Ma) oceanic lithosphere than the Canary Islands. However, we cannot preclude that this complex SRC pattern is associated with the low shear-wave velocity anomalies in the underlying mantle.

We recognize that the complex T_e pattern in the Canary region is a complex issue that deserves further analysis. We hope to address this issue in the future by exploring the effects of multiple loads through synthetic modeling.

6. Conclusions

In this work, we investigate the mechanical structure of the lithosphere beneath the ECA hotspots by calculating their effective elastic thicknesses from an analysis of the Bouguer coherence calculated using wavelet transforms.

We find that the Azores hotspot is characterized by a T_e < 10 km, whereas the Great Meteor, Cape Verde, and Madeira hotspots have intermediate T_e (15–30 km) values. In contrast, the Canary Island region is characterized by a much higher T_e (>50 km), forming the largest and most noticeable mechanical feature in the ECA.

We analyze the relation of the regional T_e distribution versus the age of the lithosphere and the temperature distribution on the basis of the plate cooling model. Averaged T_e values show the expected systematic increase with seafloor age and correlate with the depth of the 350–400°C isotherms, with an envelope of approximately 200–500°C. However, this trend is lost for oceanic lithosphere older than 130 Ma, which exhibits a T_e reduction.

When compared to the average values of the same seafloor age and with other regions in the world, we can conclude that Azores, Great Meteor, Cape Verde and Madeira have standard T_e values. In contrast, the very high T_e estimated for the Canary hotspot is found only in the oceanic lithosphere in some trenches. The comparison between the T_e distribution and the upper mantle seismic structure reveals the lack of correlation between the T_e estimated at the ECA hotspots (with the exception of Azores) and the amplitude of low shear-wave velocity anomalies in the underlying mantle. This comparison suggests a negligible effect of upper mantle temperature anomalies on the flexure of the ECA region.

The higher strength obtained for the Canary hotspot may be related to the highly depleted mantle composition in the area after melt extraction in a process that has not left a significant thermal imprint in the lithosphere. The complex T_e pattern in the Canary volcanic province may be the result of the very long, from the Late Jurassic to Recent, magmatic history of the region.

Data Availability Statement

The GEBCO_2022 Grid is available at https://www.gebco.net/data_and_products/gridded_bathymetry_data/gebco_2022/. The EGM2008 gravity model is available at https://bgi.obs-mip.fr/data-products/grids-and-models/egm2008-global-model/. The global crustal model CRUST1.0 is available at https://igppweb.ucsd.edu/~gabi/crust1.html. The global model of oceanic crustal age is available at https://www.earthbyte.org/category/resources/data-models/. The global ocean sediment thickness model GlobSed is available at https://ngdc.noaa.gov/mgg/sedthick/index.html. The surface-wave tomography model SA2019 (Celli, Lebedev, Schaeffer, Ravenna, & Gaina, 2020) is available at https://nlscelli.wixsite.com/ncseismology/sa2019. Calculations were performed using the isowave software suite (Kirby and Swain). All figures were generated using the Generic Mapping Tools (GMT) package (Wessel et al., 2019). Several maps were represented using the Scientific Colour Maps, a suite of scientific, colour-vision deficiency friendly and perceptually uniform colour maps (Crameri, 2018; Crameri et al., 2020). The effective elastic thickness results are available at Jiménez-Díaz et al. (2023).

Acknowledgments
We are grateful to editor Boris Kaus, Alexander Minakov, and four anonymous reviewers for helpful and constructive comments on previous versions of this manuscript. We would like to thank Nicolas L. Celli, Sergei Lebedev, Fei Ji, and Bo Chen for fruitful discussions on various topics presented in this article. We also thank Sophie Hanson for her help during the editorial process. A.M. Negredo and J. Fullea acknowledge support from the Spanish Ministry of Science and Innovation (PID2020-114854GB-C22). J. Fullea is supported by an Atracción Talento senior fellowship (2018-T1/AMB/11493) funded by Comunidad Autónoma de Madrid (Spain). J. Ruiz and A. Jiménez-Díaz acknowledge support from the Universidad Complutense de Madrid (4129557-FEI-EU-20-01).

References

Abdel-Monem, A., Watkins, N. D., & Gast, P. W. (1972). Potassium–argon ages, volcanic stratigraphy and geomagnetic polarity history of the Canary Islands: Tenerife, La Palma, and Hierro. *American Journal of Science*, *272*(9), 805–825. https://doi.org/10.2475/ajs.272.9.805

Ali, M. Y., Watts, A. B., & Hill, I. (2003). A seismic reflection profile study of lithospheric flexure in the vicinity of the Cape Verde Islands. *Journal of Geophysical Research*, *108*(B5), 2239. https://doi.org/10.1029/2002JB002155

Audet, P. (2014). Toward mapping the effective elastic thickness of planetary lithospheres from a spherical wavelet analysis of gravity and topography. *Physics of the Earth and Planetary Interiors*, *226*, 48–82. https://doi.org/10.1016/j.pepi.2013.09.011

Audet, P., & Bürgmann, R. (2011). Dominant role of tectonic inheritance in supercontinent cycles. *Nature Geoscience*, *4*(3), 184–187. https://doi.org/10.1038/ngeo1080

Bellas, A., Zhong, S., & Watts, A. (2020). Constraints on the rheology of the lithosphere from flexure of the Pacific Plate at the Hawaiian Islands. *Geochemistry, Geophysics, Geosystems*, *21*(2), e2019GC008819. https://doi.org/10.1029/2019GC008819

Bercovici, D., & Mulyukova, E. (2021). Evolution and demise of passive margins through grain mixing and damage. *Proceedings of the National Academy of Sciences*, *118*(4), e2011247118. https://doi.org/10.1073/pnas.2011247118

Bonatti, E. (1990). Not so hot "hot spots" in the oceanic mantle. *Science*, *250*(4977), 107–110. https://doi.org/10.1126/science.250.4977.107

Boschi, L., Becker, T. W., & Steinberger, B. (2007). Mantle plumes: Dynamic models and seismic images. *Geochemistry, Geophysics, Geosystems*, *8*(10), Q10006. https://doi.org/10.1029/2007GC001733

Burov, E. B., & Diament, M. (1995). The effective elastic thickness of (Te) continental lithosphere. What does it really means? *Journal of Geophysical Research*, *100*(B3), 3905–3927. https://doi.org/10.1029/94jb02770

Calmant, S., Francheteau, J., & Cazenave, A. (1990). Elastic layer thickening with age of the oceanic lithosphere - A tool for prediction of the age of volcanoes or oceanic crust. *Geophysical Journal International*, *100*(1), 59–67. https://doi.org/10.1111/j.1365-246x.1990.tb04567.x

Canales, J. P., & Dañobeitia, J. J. (1998). The Canary Islands swell: A coherence analysis of bathymetry and gravity. *Geophysical Journal International*, *132*(3), 479–488. https://doi.org/10.1046/j.1365-246x.1998.00448.x

Celli, N. L., Lebedev, S., Schaeffer, A. J., & Gaina, C. (2020). African cratonic lithosphere carved by mantle plumes. *Nature Communications*, *11*(1), 92. https://doi.org/10.1038/s41467-019-13871-2

Celli, N. L., Lebedev, S., Schaeffer, A. J., Ravenna, M., & Gaina, C. (2020). The upper mantle beneath the South Atlantic Ocean, South America and Africa from waveform tomography with massive data sets. *Geophysical Journal International*, *221*(1), 178–204. https://doi.org/10.1093/gji/ggz574

Chen, B., Kaban, M. K., El Khrepy, S., & Al-Arifi, N. (2015). Effective elastic thickness of the Arabian plate: Weak shield versus strong platform. *Geophysical Research Letters*, *42*(9), 3298–3304. https://doi.org/10.1002/2015GL063725

Cloetingh, S., Ziegler, P., Beekman, F., Andriessen, P., Matenco, L., Bada, G., et al. (2005). Lithospheric memory state of stress and rheology: Neotectonic controls on Europe's intraplate continental topography. *Quaternary Science Reviews*, *24*(3–4), 241–304. https://doi.org/10.1016/j.quascirev.2004.06.015

Collier, J. S., & Watts, A. B. (2001). Lithospheric response to volcanic loading by the Canary Islands: Constraints from seismic reflection data in their flexural moat. *Geophysical Journal International*, *147*(3), 660–676. https://doi.org/10.1046/j.0956-540x.2001.01506.x

Crameri, F. (2018). Scientific colour maps. *Zenodo*. https://doi.org/10.5281/zenodo.1243862

Crameri, F., Shephard, G. E., & Heron, P. J. (2020). The misuse of colour in science communication. *Nature Communications*, *11*(1), 5444. https://doi.org/10.1038/s41467-020-19160-7

Dañobeitia, J. J., Canales, J. P., & Dehghani, G. A. (1994). An estimation of the elastic thickness of the lithosphere in the Canary Archipelago using admittance function. *Geophysical Research Letters*, *21*(24), 2649–2652. https://doi.org/10.1029/94gl02552

Duncan, R. A., & Keller, R. A. (2004). Radiometric ages for basement rocks from the Emperor Seamounts, ODP Leg 197. *Geochemistry, Geophysics, Geosystems*, *5*(8), Q08L03. https://doi.org/10.1029/2004GC000704

Feraud, G., Kaneoka, I., & Allègre, J. C. (1980). K/Ar ages and stress pattern in the Azores: Geodynamic implications. *Earth and Planetary Science Letters*, *46*(2), 275–286. https://doi.org/10.1016/0012-821x(80)90013-8

Filmer, P. E., & McNutt, M. K. (1989). Geoid anomalies over the Canary Islands Group. *Marine Geophysical Researches*, *11*(2), 77–87. https://doi.org/10.1007/bf00285659

Forsyth, D. W. (1985). Subsurface loading estimates of the flexural rigidity of continental lithosphere. *Journal of Geophysical Research*, *90*, 12623–12632.

Fullea, J., Camacho, A., Negredo, A. M., & Fernández, J. (2015). The Canary Islands hot spot: New insights from 3D coupled geophysical-petrological modelling of the lithosphere and uppermost mantle. *Earth and Planetary Science Letters*, *409*, 71–88. https://doi.org/10.1016/j.epsl.2014.10.038

GEBCO Compilation Group. (2022). GEBCO 2022 Grid. https://doi.org/10.5285/e0f0bb80-ab44-2739-e053-6c86abc0289c

Geldmacher, J., Bogaard, P. V. D., Hoernle, K., & Schmincke, H.-U. (2000). New 40Ar/39Ar dating of the Madeira archipelago and hotspot track (eastern North Atlantic). *Geochemistry, Geophysics, Geosystems*, *1*(2), 1008. https://doi.org/10.1029/1999GC000018

Geldmacher, J., Hoernle, K., Van den Bogaard, P., Zankl, G., & Garbe-Schönberg, D. (2001). Earlier history of the C70-Ma-old Canary hotspot based on the temporal and geochemical evolution of the Selvagen archipelago and neighboring seamounts in the eastern north Atlantic. *Journal of Volcanology and Geothermal Research*, *111*(1–4), 55–87. https://doi.org/10.1016/s0377-0273(01)00220-7

Geldmacher, J., Hoernle, K., Van den Bogaard, P., Duggen, S., & Werner, R. (2005). New Ar-40/Ar-39 age and geochemical data from seamounts in the Canary and Madeira volcanic provinces: Support for the mantle plume hypothesis. *Earth and Planetary Science Letters*, *237*(1–2), 85–101. https://doi.org/10.1016/j.epsl.2005.04.037

Gente, P., Dyment, J., Maia, M., & Goslin, J. (2003). Interaction between the Mid-Atlantic Ridge and the Azores hot spot during the last 85 Myr: Emplacement and rifting of the hot spot-derived plateaus. *Geochemistry, Geophysics, Geosystems*, *4*(10), 8514. https://doi.org/10.1029/2003gc000527

Grotzinger, J., & Royden, L. (1990). Elastic strength of the Slave craton at 1.9 Gyr and implications for the thermal evolution of the continents. *Nature*, *347*(6288), 64–66. https://doi.org/10.1038/347064a0

Guillou, H., Carracedo, J. C., Pérez Torrado, F., & Rodríguez Badiola, E. (1996). K-Ar ages and magnetic stratigraphy of a hotspot-induced, fast grown oceanic island: El Hierro, Canary Islands. *Journal of Volcanology and Geothermal Research*, *73*(1–2), 141–155. https://doi.org/10.1016/0377-0273(96)00021-2

Hasterok, D., Halpin, J. A., Collins, A. S., Hand, M., Kreemer, C., Gard, M. G., & Glorie, S. (2022). New maps of global geological provinces and tectonic plates. *Earth-Science Reviews*, *231*, 104069. https://doi.org/10.1016/j.earscirev.2022.104069

Holik, J. S., Rabinowitz, P. D., & Austin, J. A. (1991). Effects of Canary hotspot volcanism on structure of oceanic crust off Morocco. *Journal of Geophysical Research*, *96*, 12039–12067. https://doi.org/10.1029/91jb00709

Hunter, J., & Watts, A. B. (2016). Gravity anomalies, flexure and mantle rheology seaward of circum-Pacific trenches. *Geophysical Journal International*, *207*(1), 288–316. https://doi.org/10.1093/gji/ggw275

Ito, G., Shen, Y., Hirth, G., & Wolfe, C. J. (1999). Mantle flow, melting, and dehydration of the Iceland mantle plume. *Earth and Planetary Science Letters*, *165*(1), 81–96. https://doi.org/10.1016/s0012-821x(98)00216-7

Jackson, M. G., Becker, T. W., & Steinberger, B. (2021). Spatial characteristics of recycled and primordial reservoirs in the deep mantle. *Geochemistry, Geophysics, Geosystems*, *22*(3), e2020GC009525. https://doi.org/10.1029/2020GC009525

Ji, F., Zhang, Q., Zhou, X., Bai, Y., & Li, Y. (2020). Effective elastic thickness of Zealandia and its implications for lithospheric deformation. *Gondwana Research*, *86*, 46–59. https://doi.org/10.1016/j.gr.2020.05.008

Jiménez-Díaz, A., Negredo, A. M., Kirby, J. F., Sánchez-Pastor, P., Fullea, J., Ruiz, J., et al. (2023). ECA effective elastic thickness archive [Dataset]. Zenodo. https://doi.org/10.5281/zenodo.7643399

Jiménez-Díaz, A., Ruiz, J., Pérez-Gussinyé, M., Kirby, J. F., Álvarez-Gómez, J. A., Tejero, R., & Capote, R. (2014). Spatial variations of effective elastic thickness of the lithosphere in Central America and surrounding regions. *Earth and Planetary Science Letters*, *391*, 55–66. https://doi.org/10.1016/j.epsl.2014.01.042

Kaban, M. K., Chen, B., Tesauro, M., Petrunin, A. G., El Khrepy, S., & Al-Arifi, N. (2018). Reconsidering effective elastic thickness estimates by incorporating the effect of sediments: A case study for Europe. *Geophysical Research Letters*, *45*(18), 9523–9532. https://doi.org/10.1029/2018GL079732

Kaislaniemi, L., & van Hunen, J. (2014). Dynamics of lithospheric thinning and mantle melting by edge-driven convection: Application to Moroccan Atlas Mountains. *Geochemistry, Geophysics, Geosystems*, *15*(8), 3175–3189. https://doi.org/10.1002/2014gc005414

Kalnins, L. M. (2011). *Spatial variations in the effective elastic thickness of the lithosphere and their tectonic implications*. Ph.D. Thesis. University of Oxford.

Kalnins, L. M., & Watts, A. B. (2009). Spatial variations in effective elastic thickness in the Western Pacific Ocean and their implications for Mesozoic volcanism. *Earth and Planetary Science Letters*, *286*(1–2), 89–100. https://doi.org/10.1016/j.epsl.2009.06.018

King, S. D., & Ritsema, J. (2000). African hot spot volcanism: Small-scale convection in the upper mantle beneath cratons. *Science*, *290*(5494), 1137–1140. https://doi.org/10.1126/science.290.5494.1137

Kirby, J. F. (2014). Estimation of the effective elastic thickness of the lithosphere using inverse spectral methods: The state of the art. *Tectonophysics*, *631*, 87–116. https://doi.org/10.1016/j.tecto.2014.04.021

Kirby, J. F. (2022). Spectral methods for the estimation of the effective elastic thickness of the lithosphere. In *The advances in geophysical and environmental mechanics and mathematics series* (p. 458). Springer-Nature.

Kirby, J. F., & Swain, C. J. (2004). Global and local isostatic coherence from the wavelet transform. *Geophysical Research Letters*, *31*(24), L24608. https://doi.org/10.1029/2004GL021569

Kirby, J. F., & Swain, C. J. (2006). Mapping the mechanical anisotropy of the lithosphere using a 2D wavelet coherence, and its application to Australia. *Physics of the Earth and Planetary Interiors*, *158*(2–4), 122–138. https://doi.org/10.1016/j.pepi.2006.03.022

Kirby, J. F., & Swain, C. J. (2008). An accuracy assessment of the fanwavelet coherence method for elastic thickness estimation. *Geochemistry, Geophysics, Geosystems*, *9*(3), Q03022. (Correction. (2008). Geochemistry Geophysics Geosystems, 9(5), Q05021). https://doi.org/10.1029/2007gc001773

Kirby, J. F., & Swain, C. J. (2009). A reassessment of spectral Te estimation in continental interiors: The case of North America. *Journal of Geophysical Research*, *114*(B8), B08401. https://doi.org/10.1029/2009jb006356

Kirby, J. F., & Swain, C. J. (2011). Improving the spatial resolution of effective elastic thickness estimation with the fan wavelet transform. *Computers and Geosciences*, *37*(9), 1345–1354. https://doi.org/10.1016/j.cageo.2010.10.008

Kirby, J. F., & Swain, C. J. (2013). Power spectral estimates using two-dimensional Morlet-fan wavelets with emphasis on the long wavelengths: Jackknife errors, bandwidth resolution and orthogonality properties. *Geophysical Journal International*, *194*(1), 78–99. https://doi.org/10.1093/gji/ggt103

Laske, G., Masters, G., Ma, Z., & Pasyanos, M. (2013). Update on CRUST1.0 – A 1-degree global model of Earth's crust. *Geophysical Research Abstracts*, *15*. Abstract EGU2013-2658.

Levitt, D. A., & Sandwell, D. T. (1995). Lithospheric bending at subduction zones based on depth soundings and satellite gravity. *Journal of Geophysical Research*, *100*(B1), 379–400. https://doi.org/10.1029/94jb02468

Liu, X., & Zhao, D. (2021). Seismic evidence for a plume-modified oceanic lithosphere–asthenosphere system beneath Cape Verde. *Geophysical Journal International*, *225*, 872Â–886. https://doi.org/10.1093/gji/ggab012

Llanes, P. (2006). *Estructura de la litosfera en el entorno de las Islas Canarias a partir del análisis gravimétrico e isostáticoimplicaciones geodinámicas*. Ph.D. Thesis. Universidad Compluense de Madrid.

Lu, Z., Audet, P., Li, C. F., Zhu, S., & Wu, Z. (2021). What controls effective elastic thickness of the lithosphere in the Pacific Ocean? *Journal of Geophysical Research: Solid Earth*, *126*(3), e2020JB021074. https://doi.org/10.1029/2020JB021074

Luis, J. F., & Neves, M. C. (2006). The isostatic compensation of the Azores Plateau: A 3D admittance and coherence analysis. *Journal of Volcanology and Geothermal Research*, *156*(1–2), 10–22. https://doi.org/10.1016/j.jvolgeores.2006.03.010

Manjón-Cabeza Córdoba, A., & Ballmer, M. (2021). The role of edge-driven Convection in the generation of volcanism I: A 2D systematic study, solid Earth discuss. *Solid Earth*, *12*(3), 613–632. https://doi.org/10.5194/se-12-613-2021

McAdoo, D. C., & Martin, C. F. (1984). Seasat observation of geoid anomalies due to subducting slabs. *Journal of Geophysical Research*, *87*, 8684–8692.

McDougall, I., & Schmincke, H. U. (1976). Geochronology of Gran Canaria, Canary Islands: Age of shield building volcanism and other magmatic phases. *Bulletin of Volcanology*, *40*, 1–21. https://doi.org/10.1007/bf02599829

McKenzie, D. (2003). Estimating Te in the presence of internal loads. *Journal of Geophysical Research*, *108*(B9), 2438.

McKenzie, D., & Bowin, C. (1976). Relationship between bathymetry and gravity in the Atlantic Ocean. *Journal of Geophysical Research*, *81*(11), 1903–1915. https://doi.org/10.1029/jb081i011p01903

McKenzie, D., & Fairhead, D. (1997). Estimates of the effective elastic thickness of the continental lithosphere from Bouguer and free air gravity anomalies. *Journal of Geophysical Research*, *102*(B12), 27523–27552. https://doi.org/10.1029/97JB02481

McNutt, M. (1988). Thermal and mechanical properties of the Cape Verde Rise. *Journal of Geophysical Research*, *93*(B4), 2784–2794. https://doi.org/10.1029/jb093ib04p02784

Monnereau, M., & Cazenave, A. (1990). Depth and geoid anomalies over oceanic hotspot swells: A global survey. *Journal of Geophysical Research*, *95*(B10), 15429–15438. https://doi.org/10.1029/JB095iB10p15429

Montelli, R., Nolet, G., Dahlen, F. A., & Masters, G. (2006). A catalogue of deep mantle plumes: New results from finite-frequency tomography. *Geochemistry, Geophysics, Geosystems*, *7*(11), Q11007. https://doi.org/10.1029/2006GC001248

Mooney, W. D., & Kaban, M. K. (2010). The North American upper mantle: Density, composition, and evolution. *Journal of Geophysical Research*, *115*(B12), B12424. https://doi.org/10.1029/2010jb000866

Mulyukova, E., & Bercovici, D. (2018). Collapse of passive margins by lithospheric damage and plunging grain size. *Earth and Planetary Science Letters*, *484*, 341–352. https://doi.org/10.1016/j.epsl.2017.12.022

Negredo, A. M., van Hunen, J., Rodríguez-González, J., & Fullea, J. (2022). On the origin of the Canary Islands: Insights from mantle convection modelling. *Earth and Planetary Science Letters*, *584*, 117506. https://doi.org/10.1016/j.epsl.2022.117506

Neumann, E.-R., Wulff-Pedersen, E., Johnsen, K., Andersen, T., & Krogh, E. (1995). Petrogenesis of spinel harzburgite and dunite suite xenoliths from Lanzarote, eastern Canary Islands: Implications for the upper mantle. *Lithos*, *35*(1–2), 83–107. https://doi.org/10.1016/0024-4937(95)91153-z

Neumann, E.-R., Wulff-Pedersen, E., Pearson, N., & Spencer, E. (2002). Mantle xenoliths from Tenerife (Canary Islands): Evidence for reactions between mantle peridotites and silicic carbonatite melts inducing Ca metasomatism. *Journal of Petrology*, *43*(5), 825–857. https://doi.org/10.1093/petrology/43.5.825

Parsons, B., & Sclater, J. G. (1977). An analysis of the variation of ocean floor bathymetry and heat flow with age. *Journal of Geophysical Research*, *82*(5), 803–827. https://doi.org/10.1029/jb082i005p00803

Pavlis, N. K., Holmes, S. A., Kenyon, S. C., & Factor, J. K. (2008). *An Earth gravitational model to degree 2160: EGM2008*. EGU General Assembly 2008.

Pérez-Gussinyé, M., Lowry, A. R., Watts, A. B., & Velicogna, I. (2004). On the recovery of effective elastic thickness using spectral methods: Examples from synthetic data and from the Fennoscandian Shield. *Journal of Geophysical Research*, *109*(B10), B10409. https://doi.org/10.1029/2003JB002788

Pérez-Gussinyé, M., Metois, M., Fernández, M., Vergés, J., Fullea, J., & Lowry, A. R. (2009). Effective elastic thickness of Africa and its relationship to other proxies for lithospheric structure and surface tectonics. *Earth and Planetary Science Letters*, *287*(1–2), 152–167. https://doi.org/10.1016/j.epsl.2009.08.004

Press, W. H., Teukolsky, S. A., Vetterling, W. T., & Flannery, B. P. (1992). *Numerical recipes in Fortran 77* (2nd ed.). Cambridge University Press.

Rao, D. B., & Babu, N. R. (1991). A Fortran-77 computer program for three-dimensional analysis of gravity anomalies with variable density contrast. *Computational Geosciences*, *17*(5), 655–667. https://doi.org/10.1016/0098-3004(91)90037-e

Ratheesh-Kumar, R. T., Ishwar-Kumar, C., Windley, B. F., Razakamanana, T., Nair, R. R., & Sajeev, K. (2015). India–Madagascar paleo-fit based on flexural isostasy of their rifted margins. *Gondwana Research*, *28*(2), 581–600. https://doi.org/10.1016/j.gr.2014.06.008

Ratheesh-Kumar, R. T., & Xiao, W. (2018). Effective elastic thickness along the conjugate passive margins of India, Madagascar and Antarctica: A re-evaluation using the Hermite multitaper Bouguer coherence application. *Journal of Asian Earth Sciences*, *157*, 40–56. https://doi.org/10.1016/j.jseaes.2017.03.019

Ribeiro, L. P., Martins, S., Hildenbrand, A., Madureira, P., & Mata, J. (2017). The genetic link between the Azores Archipelago and the Southern Azores Seamount Chain (SASC): The elemental, isotopic and chronological evidences. *Lithos*, *294–295*, 133–146. https://doi.org/10.1016/j.lithos.2017.08.019

Sartori, R., Torelli, L., Zitellini, N., Peis, D., & Lodolo, E. (1994). Eastern segment of the Azores–Gibraltar line (central-eastern Atlantic): An oceanic plate boundary with diffuse compressional deformation. *Geology*, *22*(6), 555–558. https://doi.org/10.1130/0091-7613(1994)022<0555:esotag>2.3.co;2

Schaeffer, A., & Lebedev, S. (2013). Global shear speed structure of the upper mantle and transition zone. *Geophysical Journal International*, *194*(1), 417–449. https://doi.org/10.1093/gji/ggt095

Seton, M., Müller, R. D., Zahirovic, S., Williams, S., Wright, N. M., Cannon, J., et al. (2020). A global data set of present-day oceanic crustal age and seafloor spreading parameters. *Geochemistry, Geophysics, Geosystems*, *21*(10), e2020GC009214. https://doi.org/10.1029/2020GC009214

Shi, X., Kirby, J., Yu, C., Jiménez-Díaz, A., & Zhao, J. (2017). Spatial variations in the effective elastic thickness of the lithosphere in Southeast Asia. *Gondwana Research*, *42*, 49–62. https://doi.org/10.1016/j.gr.2016.10.005

Simon, N. S. C., Neumann, E.-R., Bonadiman, C., Coltorti, M., Delpech, G., Grégoire, M., & Widom, E. (2008). Ultra-refractory domains in the Oceanic mantle lithosphere sampled as mantle xenoliths at Ocean Islands. *Journal of Petrology*, *49*(6), 1223–1251. https://doi.org/10.1093/petrology/egn023

Stark, C. P., Stewart, J., & Ebinger, C. J. (2003). Wavelet transform mapping of effective elastic thickness and plate loading: Validation using synthetic data and application to the study of southern African tectonics. *Journal of Geophysical Research*, *108*(B12), 2558. https://doi.org/10.1029/2001jb000609

Straume, E. O., Gaina, C., Medvedev, S., Hochmuth, K., Gohl, K., Whittaker, J. M., et al. (2019). GlobSed: Updated total sediment thickness in the world's oceans. *Geochemistry, Geophysics, Geosystems*, *20*(4), 1756–1772. https://doi.org/10.1029/2018GC008115

Swain, C. J., & Kirby, J. F. (2006). An effective elastic thickness map of Australia from wavelet transforms of gravity and topography using Forsyth's method. *Geophysical Research Letters*, *33*(2), L02314. https://doi.org/10.1029/2005GL025090

Swain, C. J., & Kirby, J. F. (2021). Effective elastic thickness map reveals subglacial structure of East Antarctica. *Geophysical Research Letters*, *48*(4), e2020GL091576. https://doi.org/10.1029/2020GL091576

Tesauro, M., Kaban, M. K., & Mooney, W. D. (2015). Variations of the lithospheric strength and elastic thickness in North America. *Geochemistry, Geophysics, Geosystems*, *16*(7), 2197–2220. https://doi.org/10.1002/2015GC005937

van den Bogaard, P. (2013). The origin of the Canary Island seamount province – New ages of old seamounts. *Scientific Reports*, *3*(1), 2107. https://doi.org/10.1038/srep02107

Verhoef, J. (1984). *A geophysical study of the Atlantis-Meteor seamount complex*. Ph.D. Thesis (Vol. 38, p. 153). University of Utrecht. *Geol. Ultrajectina*.

Watts, A. B. (1978). An analysis of isostasy in the world's oceans 1. Hawaiian-Emperor Seamount Chain. *Journal of Geophysical Research*, *83*(B12), 5989–6004. https://doi.org/10.1029/JB083iB12p05989

Watts, A. B. (1994). Crustal structure, gravity anomalies and flexure of the lithosphere in the Canary Islands. *Geophysical Journal International*, *119*(2), 648–666. https://doi.org/10.1111/j.1365-246x.1994.tb00147.x

Watts, A. B. (2001). *Isostasy and flexure of the lithosphere*. Cambridge University Press.

Watts, A. B., & Burov, E. B. (2003). Lithospheric strength and its relation to the elastic and seismogenetic layer thickness. *Earth and Planetary Science Letters*, *213*(1–2), 113–131. https://doi.org/10.1016/s0012-821x(03)00289-9

Watts, A. B., Cochran, J. R., & Selzer, G. (1975). Gravity anomalies and flexure of the lithosphere: A three-dimensional study of the Great Meteor Seamount, N.E. Atlantic. *Journal of Geophysical Research*, *80*(11), 1391–1398. https://doi.org/10.1029/jb080i011p01391

Watts, A. B., Peirce, C., Collier, J., Dalwood, R., Canales, J., & Henstock, T. (1997). A seismic study of lithospheric flexure in the vicinity of Tenerife, Canary Islands. *Earth and Planetary Science Letters*, *146*(3–4), 431–447. https://doi.org/10.1016/s0012-821x(96)00249-x

Watts, A. B., Sandwell, D. T., Smith, W. H. F., & Wessel, P. (2006). Global gravity, bathymetry, and the distribution of submarine volcanism through space and time. *Journal of Geophysical Research*, *111*(B8), B08408. https://doi.org/10.1029/2005JB004083

Watts, A. B., Tenbrink, U. S., Buhl, P., & Brocher, T. M. (1985). A multichannel seismic study of lithospheric flexure across the Hawaiian–Emperor Seamount Chain. *Nature*, *315*(6015), 105–111. https://doi.org/10.1038/315105a0

Watts, A. B., & Zhong, S. (2000). Observations of flexure and the rheology of oceanic lithosphere. *Geophysical Journal International*, *142*(3), 855–875. https://doi.org/10.1046/j.1365-246x.2000.00189.x

Wessel, P. (2001). Global distribution of seamounts inferred from gridded Geosat/ERS-1 altimetry. *Journal of Geophysical Research*, *106*, 19431–19441. https://doi.org/10.1029/2000jb000083

Wessel, P., & Haxby, W. F. (1990). Thermal stresses, differential subsidence, and flexure at oceanic fracture zones. *Journal of Geophysical Research*, *95*(B1), 375–391. https://doi.org/10.1029/JB095iB01p00375

Wessel, P., Luis, J. F., Uieda, L., Scharroo, R., Wobbe, F., Smith, W. H. F., & Tian, D. (2019). The Generic mapping Tools version 6. *Geochemistry, Geophysics, Geosystems*, *20*(11), 5556–5564. https://doi.org/10.1029/2019GC008515

Wulff-Pedersen, E., Neumann, E.-R., & Jensen, B. (1996). The upper mantle under La Palma, Canary Islands: Formation of Si–K–Na-rich melt and its importance as a metasomatic agent. Contrib. *Mineralogy and Petrology*, *125*(2–3), 113–139. https://doi.org/10.1007/s004100050210

Yang, A., & Fu, Y. (2018). Estimates of effective elastic thickness at subduction zones. *Journal of Geodynamics*, *117*, 75–87. https://doi.org/10.1016/j.jog.2018.04.007

Young, R., & Hill, I. A. (1986). An estimate of the effective elastic thickness of the Cape Verde Rise. *Journal of Geophysical Research*, *91*(B5), 4854–4867. https://doi.org/10.1029/jb091ib05p04854

Yu, C., Xu, M., Kirby, J. F., Shi, X., & Jiménez-Díaz, A. (2022). Spatial variations of the effective elastic thickness and internal load fraction in the Cascadia subduction zone. *Geophysical Journal International*, *229*(1), 487–504. https://doi.org/10.1093/gji/ggab495

Zaczek, K., Troll, V. R., Cachao, M., Ferreira, J., Deegan, F. M., Carracedo, J. C., et al. (2015). Nannofossils in 2011 El Hierro eruptive products reinstate plume model for Canary Islands. *Scientific Reports*, *5*(1), 7945. https://doi.org/10.1038/srep07945

Zhang, Y.-S., & Tanimoto, T. (1993). High-resolution global upper mantle structure and plate tectonics. *Journal of Geophysical Research*, *98*(B6), 9793–9823. https://doi.org/10.1029/93jb00148

Zhao, D. (2007). Seismic images under 60 hotspots: Search for mantle plumes. *Gondwana Research*, *12*(4), 335–355. https://doi.org/10.1016/j.gr.2007.03.001

Zheng, Y., & Arkani-Hamed, J. (2002). Rigidity of the Atlantic oceanic lithosphere beneath New England seamounts. *Tectonophysics*, *359*(3–4), 359–369. https://doi.org/10.1016/s0040-1951(02)00533-4

Zhong, S. J., & Watts, A. B. (2013). Lithospheric deformation induced by loading of the Hawaiian Islands and its implications for mantle rheology. *Journal of Geophysical Research: Solid Earth*, *118*(11), 6025–6048. https://doi.org/10.1002/2013JB010408

References From the Supporting Information

Macario, A., Malinverno, A., & Haxby, W. F. (1995). On the robustness of elastic thickness estimates obtained using the coherence method. *Journal of Geophysical Research*, *100*(D8), 15163–15172. https://doi.org/10.1029/95jb00980